PTEN restrains SHH medulloblastma growth through cell autonomous and nonautonomous mechanisms

Zhimin Lao[1], Salsabiel El Nagar[1,3,#], Yinwen Liang[1,#], Daniel N. Stephen[1], Alexandra L. Joyner[1,2*]

[1]Developmental Biology Program, Sloan Kettering Institute, Memorial Sloan Kettering Cancer Center, New York 10065, NY, USA

[2]Biochemistry, Cell and Molecular Biology Program, Weill Cornell Graduate School of Medical Sciences, New York 10021, NY, USA

[3]Current address: Sophrosyne Bio, New York, NY, USA

[#]These authors contributed equally to the work

*Correspondence to:
Alexandra L. Joyner
Developmental Biology Program
Sloan Kettering Institute
1275 York Avenue, Box 511
New York, NY 10065, USA
Office: 212-639-3962
Email: joynera@mskcc.org

Abstract

A third of patients with the pediatric cerebellar tumor Medulloblastoma (MB) have mutations that activate Sonic hedgehog (SHH) signaling (SHH-MB subgroup). The contribution of secondary mutations to tumor severity, however is not clear. *PTEN* mutations are enriched in the SHH-1 subtype that has the lowest survival rate. Widespread heterozygous loss of *Pten* in two SHH-MB mouse models increases penetrance and excellerates onset of differentiated tumors. We delineated cellular and transcriptional changes that accelerate tumor growth and cause differentiation using a sporadic SHH-MB mouse model expressing oncogenic SmoM2 in rare cerebellar granule cell precursors (GCPs) and scRNA-seq analysis. Homozygous but not heterozygous sporadic loss of *Pten* resulted in rapid acceleration of tumor growth and end stage disease by 40 days, compared to ~25% survival in control *SmoM2* mice at 100 days. Heterozygous *PTEN* mutations therefore should negatively impact disease outcome primarily with germline mutations. Loss of *Pten* in normal or SmoM2-expressing GCPs increased proliferation and enhanced progenitor state initially but by 12 days *Pten* mutant *SmoM2* tumors were highly differentiated due to increased survival of non-proliferating GCPs. Furthermore, macrophage infiltration and cytotoxicity were reduced in differentiated regions of tumors lacking *Pten*, indicating cell nonautonomous changes also contribute to accelerated tumor growth.

Introduction

Medulloblastoma (MB) is a brain tumor seen mainly in pediatric patients and which has four molecular subgroups, WNT, SHH, Group 3 and Group 4[1]. The Sonic hedgehog subgroup of MB (SHH-MB) constitutes approximately 30% of MB and is characterized by mutations that constitutively activate SHH-signaling. Most SHH-MBs have one of four types of mutations that activate SHH-signaling: activating mutations in *SMO*, loss of function mutations in the pathway inhibitors *PTCH1* and *SUFU* or loss of *TP53* in association with amplification of the pathway effectors *GLI2* or *MYCN*. SHH-MB is further divided into four subtypes based on molecular, biological and clinical parameters[2-6]. The work on SHH-MB subtypes has highlighted that particular secondary mutations likely contribution to tumor severity. For example, heterozygous *PTEN* and *KMT2D* loss-of-function mutations are enriched in the SHH-1 or beta subtype which has the lowest overall survival rate and highest frequency of metastasis and occurs primarily in infants (<4 years). Our recent work on the chromatin modifier *KMT2D* using two SHH-MB mouse models showed that when one or two copies of *Kmt2d* are deleted, not only is there a nearly two-fold increase in tumor penetrance with a Classic tumor cytoarchitecture (highly proliferative), but strikingly a near 100% penetrance of spinal cord metastasis and hindbrain invasion[7]. The transcriptional/chromatin landscape of mouse *Kmt2d* mutant SHH-MB primary and metastatic tumors was found to be shifted towards decreased expression of neural differentiation genes and an increase in oncogenes seen in more aggressive tumors compared to tumors with intact *Kmt2d*[7]. Thus, mouse models support the clinical data that loss of *KMT2D* contributes to more aggressive disease.

The gene encoding the dual specificity phosphatase *PTEN* (Phosphatase and TENsin homolog deleted on chromosome 10), is one of the most frequently mutated tumor suppressor genes in human cancers[8], and is mutated in ~5% of SHH-MB[3]. PTEN regulates an array of cellular functions, including cell survival, proliferation and metabolism through attenuating phosphoinositide-3 kinase (PI3K-AKT) signaling and genome stability through nuclear functions. Recent work showed that PTEN also can be secreted and act in a cell nonautonomous manner[9-11]. PTEN is secreted by tumor cells via binding to TMED10 and then binds to PLXDC2 on tumor associated macrophages (TAMs) and induces inflammatory status through triggering JAK2-STAT signaling, thus contributing to the tumor suppressor function of PTEN. Mouse models of SHH-MB indicate loss of *Pten* increases tumor incidence, but the underlying cell autonomous and nonautonomous reasons and impact on metastasis are not as clear[12, 13].

90 SHH-medulloblastoma arises in *Atoh1*-expressing granule cell precursors (GCPs) on the
91 surface of the developing cerebellum. These precursor cells are dependent on SHH-signaling for
92 their sustained proliferation and major expansion during the first two weeks after birth in mice[14-
93 16]. In a mouse model of SHH-MB in which a *NeuroD2* promoter drives expression of an oncogenic
94 form of SMO (SmoA1) in the GCP-lineage, heterozygous loss of *Pten* in all cells (null mutation)
95 or conditional knock-out in Nestin-expressing cells, which includes all cerebellar cells[17], leads to
96 increased penetrance and earlier onset of tumor formation with no increase in metastasis[12].
97 Whereas most mouse models of SHH-MB have a classic (highly proliferative) histology, the *Pten*
98 heterozygous mutant tumors have a nodular character with extensive regions of neural
99 differentiation (NeuN+ cells) and an apparent decrease in cell death and increase in angiogenesis.
100 In a mouse SHH-MB conditional model in which *Ptch1* is homozygously deleted at embryonic day
101 14 (E14) in all GCPs (*Atoh1-Cre*), additional homozygous loss of *Pten* leads to rapid tumor
102 formation, and heterozygous loss leads to a slightly more aggressive phenotype than *Ptch1* loss
103 alone[13]. Similar to *NeuroD2*-SmoA1 tumors, in *Ptch1* mutant tumors *Pten* loss causes highly
104 differentiated tumors with decreased cell death. In a mutagenic screen for increased SHH-MB
105 penetrance and metastasis using a Sleeping beauty transposon approach in mice with
106 heterozygous mutations in *Ptch1* or *Trp53*, insertions found in tumors with spinal cord metastasis
107 were associated with mutations in *Pten*, *Akt2, Pik3R* and *Igf2,* implicating increased PI3K
108 signaling in metastasis[18]. Consist with this, in a mouse model where *Shh* is expressed in GCPs,
109 additional expression of an activated form of AKT increases tumor incidence and spinal cord
110 metastasis[18, 19]. Data from human tumors support that a reduction in *PTEN* protein enhances
111 tumor progression, since SHH-MB human patients with reduced or no PTEN protein have a worse
112 overall survival[12]. However, no correlation was seen between PTEN protein level and histology or
113 metastasis. Thus, several questions remain as to whether *Pten* loss increases metastasis, what
114 accounts for the faster growth and a more differentiated cellular phenotype in mouse *Pten* mutant
115 SHH-MBs and why only in some models *Pten* heterozygous loss is sufficient to greatly enhance
116 tumor progression.
117 We addressed these questions by comparing tumor progression and spinal cord
118 metastasis in a sporadic mouse model of SHH-MB in which rare GCPs are induced to express an
119 oncogenic form of SMO, SmoM2, at postnatal day 0 (P0) and have deletion of one or both copies
120 of *Pten*. We found that only homozygous loss of *Pten* combined with SmoM2 expression
121 enhances tumor progression in this sporadic model, and metastasis is not increased.
122 Furthermore, the differentiated phenotype of the tumors is primarily due to a specific decrease in
123 cell death of non-proliferative cells in the tumors, whereas cell death is as high in regions of high

124 proliferation as in *SmoM2* tumors with normal *Pten* or heterozygous loss of *Pten*. Loss of *Pten* in
125 normal GCPs, or those expressing SmoM2, leads to a mild initial increase in the proliferation
126 index, indicating a cell autonomous function of PTEN in reducing proliferation. Single cell RNA-
127 sequencing (scRNA-seq) analysis revealed that proliferating tumor cells that lack *Pten* not only
128 have the expected increase in mTOR signaling, but also have altered expression of genes
129 involved in neural differentiation and down regulation of inflammatory and interferon alpha
130 response genes. Homozygous loss of *Pten* in GCPs also leads to a major decrease in infiltration
131 of macrophages into tumors and an altered transcriptome indicating reduced cytotoxicity,
132 revealing a possible cell nonautonomous function of PTEN that normally reduces tumor
133 progression.
134

135 ## Results

136 **_PTEN_ mutations co-occur with mutations that activate SHH-signaling in human SHH-MB**
137 Using the cBioPortal[20, 21] and a dataset of 127 patient samples considered to be SHH-MB[3], we
138 determined whether patients with mutations that activate SHH-signaling have *PTEN* mutations.
139 4.3% of the 127 samples had a mutation in *PTEN* and furthermore 4/5 of the mutations co-
140 occurred with mutations that activate SHH-signaling (*Ptch1*, *SUFU* or *SMO*; **Fig. 1A**). Thus,
141 although the *PTEN* mutations were detected in a low percentage of patient tumors, *PTEN* appears
142 to be predominantly mutated in SHH-MB along with mutations that activate SHH-signaling.
143

144 **Homozygous loss of _Pten_ in sporadic SHH-MB accelerates growth and increases**
145 **penetrance to 100%**
146 We next used our mosaic mutant technique (MASTR)[22] to test the impact of lowering *Pten* in a
147 sporadic mouse model of SHH-MB. The approach involves inducing expression of an oncogenic
148 form of the SHH receptor SMO (SmoM2) and eGFP in ~20,000 GCPs (~0.1%) at P0 (**Fig. 1B**)[22-
149 24]. The model allows penetrance and survival time to be determined since less than 75% of mutant
150 mice die by 100 days. Using the model, we asked whether loss of one or both copies of *Pten*[25] in
151 rare GCPs-expressing SmoM2 changes the survival curves of mice by comparing *Atoh1-*
152 *FlpoER/+*; *R26*$^{MASTR/LSL\text{-}SmoM2}$ mice (referred to as *SmoM2*) to *Atoh1-FlpoER/+*; *R26*$^{MASTR/LSL\text{-}SmoM2}$;
153 *Pten*$^{fl/fl}$ (referred to as *SmoM2-Pten*$^{fl/fl}$) and *Atoh1-FlpoER/+*; *R26*$^{MASTR/LSL\text{-}SmoM2}$; *Pten*$^{fl/+}$ (referred
154 to as *SmoM2-Pten*$^{fl/+}$) mice administered tamoxifen at P0 (**Fig. 1B**). Strikingly, all *SmoM2-Pten*$^{fl/fl}$
155 mice succumbed to disease between P20 and P40, whereas *SmoM2* and *SmoM2-Pten*$^{fl/+}$ mice
156 began dying at ~P40 and by P100 ~25% of mice of both genotypes survived (**Fig. 1C**). Thus, loss
157 of both *Pten* alleles is required to accelerate tumor progression in a mosaic *SmoM2* model of

158 SHH-MB, unlike a *SmoA2* model with germline or broad deletion of *Pten* in the cerebellum where
159 heterozygous deletion is sufficient[12].
160
161 **Homozygous and heterozygous loss of *Pten* does not increase metastasis to the spinal**
162 **cord in *SmoM2* SHH-MB**
163 Given the different reported findings as to whether *Pten* loss increases metastasis in mouse
164 models of SHH-MB, we asked whether in our sporadic *SmoM2* mice loss of *Pten* alters the
165 frequency of spinal cord metastasis when mice show signs of brain tumor disease. Coronal spinal
166 cord sections of each mouse (n=55-138 sections per mouse) were analyzed by cytology for the
167 presence of spinal cord metastasis and tumors were confirmed with immunohistochemical (IHC)
168 staining for GFP, Ki67 and PTEN (**Figure 1–figure supplement 1A-C**). Quantification of the
169 percentage of mice that had at least 2 sections with more than a few tumor cells showed a similar
170 tumor incidence between the three genotypes (*SmoM2*: 64%, n=11; *SmoM2-Pten*$^{fl/+}$: 69%, n=13;
171 *SmoM2-Pten*$^{fl/fl}$: 58%, n=12). Furthermore, quantification of the percentage of spinal cord sections
172 per mouse with tumor cells showed no difference between the *Pten* mutant tumors and *SmoM2*
173 (**Figure 1–figure supplement 1D**). Likewise, measuring the area of the tumors did not detect a
174 difference in metastatic disease when *Pten* was lowered or deleted (**Figure 1–figure supplement**
175 **1E, F**). Thus, in mouse sporadic *SmoM2* SHH-MB, heterozygous or homozygous loss of *Pten*
176 does not appear to increase spinal cord metastasis.
177
178 ***Pten* loss in a *SmoM2* sporadic mouse model of SHH-MB induces highly differentiated**
179 **tumors**
180 Hematoxylin and eosin (H&E) staining of primary tumor sections indicated that homozygous loss
181 of *Pten* results in tumors with decreased cellularity (**Fig1 D-F**). IHC staining of tumor sections at
182 end stage confirmed that most tumor cells expressed GFP (**Fig 1. G-I**) and only *SmoM2-Pten*$^{fl/fl}$
183 tumors lacked PTEN (**Fig 1. J-L**) and had strong Phospho-AKT (pAKT) (**Fig 1. M-O**) and pS6
184 staining (**Figure 2–figure supplement 1A-D**), thus confirming absence of PTEN and activation
185 of mTOR (mammalian target of rapamycin) signaling only in *SmoM2-Pten*$^{fl/fl}$ tumors. Staining with
186 markers of cell proliferation (Ki67) and differentiation revealed that whereas *SmoM2* tumors
187 consisted of mostly Ki67+ cells, *SmoM2-Pten*$^{fl/fl}$ tumors were highly differentiated expressing the
188 post mitotic marker P27 and neural differentiation marker NeuN with only small areas of
189 proliferative cells (**Fig. 2A-H**). The *SmoM2* tumors had broad expression of the SHH target gene
190 *Gli1*, whereas the *SmoM2-Pten*$^{fl/fl}$ tumors expressed *Gli1* mRNA only in Ki67+ regions of the
191 tumors (**Fig. 2I-L**), which was complementary to the neural differentiation marker Synaptophysin

192 (SYP/*Syp*) that was absent from *SmoM2* tumors (**Fig. 2K-P**). Thus, despite *SmoM2* being
193 expressed in the differentiated cells of the *SmoM2-Pten*$^{fl/fl}$ tumors, SHH-signaling is down
194 regulated specifically in differentiated cells. Interestingly, in 3/9 tumors from *SmoM2-Pten*$^{fl/+}$ mice
195 some sections had patches of cells devoid of PTEN and positive for pAKT, indicating spontaneous
196 loss of the second allele of *Pten* in rare cells that expand as a coherent group (**Figure 2–figure**
197 **supplement 1E-H**). The regions without PTEN in *SmoM2-Pten*$^{fl/+}$ mice had a similar differentiated
198 phenotype (SYP+ and NeuN+) to *SmoM2-Pten*$^{fl/fl}$ tumors (**Figure 2–figure supplement 1I-K**).
199
200 ***Pten* loss protects differentiated tumor cells from cell death**
201 Mouse SHH-MB models that have a highly differentiated cytology are rare and have primarily
202 been reported in two *Pten* models[12, 13]. In a *Ptch1* mutant model of SHH-MB, it was shown that
203 proliferating tumor cells give rise to NeuN+ postmitotic tumor cells that then die at a high rate[26].
204 We therefore asked whether *Pten* loss (increased mTOR signaling) rescues the post-mitotic tumor
205 cells from death by staining for SYP or NeuN and TUNEL (**Fig. 3A-H**). *SmoM2-Pten*$^{fl/fl}$ tumors had
206 significantly less TUNEL particles in regions of high SYP labeling (SYP Hi) compared to SYP low
207 regions (**Fig. 3C-I, Figure 3–figure supplement 1**). Moreover, in the regions of low SYP, the
208 density of TUNEL staining was similar to in *SmoM2* tumors where SYP is low throughout the
209 tumor. (**Fig. 3J**). As expected, in PTEN negative patches of *SmoM2-Pten*$^{fl/+}$ tumors, TUNEL
210 staining was lower in these SYP Hi regions of differentiated cells (NeuN+) than in SYP low
211 proliferative regions (Ki67+) (**Fig. 3J,K** and **Figure 2–figure supplement 1I-L**).
212
213 **Loss of *Pten* leads to rapid cell autonomous changes in SmoM2 GCP behaviors**
214 Given how rapidly the tumors grow in the *SmoM2-Pten*$^{fl/fl}$ mice and that lethal disease occurs
215 between P20-40, we asked how early a differential growth phenotype can be seen in the three
216 genotypes. In our previous study of the effect of loss of *Kmt2d* in SHH-MB models, no difference
217 in tumor size was detected at P12 but was by P21[7]. We therefore asked whether *SmoM2-Pten*$^{fl/fl}$
218 tumors have a growth advantage over *SmoM2* tumors at P12. Staining of sagittal sections of
219 *SmoM2* tumors of the three *Pten* genotypes with EdU (1 hour pulse) and GFP to mark the
220 proliferating GCPs in the external granule cell layer (EGL) showed a massive expansion of the
221 EGL in *SmoM2-Pten*$^{fl/fl}$ mice compared to *SmoM2* mice (**Fig. 4 A-C**). Quantification of cerebellar
222 area in midline sections revealed a significant increase in *SmoM2-Pten*$^{fl/fl}$ mice compared to
223 *SmoM2* mice and *SmoM2-Pten*$^{fl/+}$ mice (**Fig. 4D**). The EGL area alone showed a 4-fold average
224 area increase in *SmoM2-Pten*$^{fl/fl}$ mice compared to *SmoM2* mice and *SmoM2-Pten*$^{fl/f+}$ mice had a
225 slight increase (<2-fold) compared to *SmoM2* mice (**Fig. 4E**). As in end stage tumors, the tumors

226 in *SmoM2-Pten*$^{fl/fl}$ mice had a significant decrease in dying cells compared to the other two
227 genotypes at P12 (**Fig, 4F-L, Fig. 4–figure supplement 1**). In large lesions with extensive
228 differentiation (NeuN+ Ki67- cells) the density of TUNEL particles was decrease in NeuN+ regions
229 compared to proliferative regions. As expected, pAKT staining was upregulated in the EGL of
230 *SmoM2-Pten*$^{fl/fl}$ mice with no detectable staining in the other two genotypes (**Fig. 4M-O**).
231
232 One prediction of our findings is that once *SmoM2* GCPs lacking *Pten* differentiate their
233 survival should be enhanced. Therefore, if proliferating GCPs are labeled and then fate mapped
234 for two days, a higher percentage of *SmoM2-Pten*$^{fl/fl}$ labeled cells should be differentiated (post-
235 mitotic) compared to in *SmoM2* mice. To test this idea, we administered one injection of BrdU into
236 P10 mice and then sacrificed them at P12 and quantified the percentage of BrdU+ cells in the
237 EGL that were Ki67- (**Fig. 4P**). As predicted, a higher percentage of BrdU+ cells in *SmoM2-Pten*$^{fl/fl}$
238 mice were Ki67- at P12 compared to *SmoM2* (**Fig. 4Q**). This result indicates that by P10 after
239 loss of *Pten* at P0, either differentiation is promoted in *SmoM2* GCPs and/or that the differentiated
240 progeny of GCPs lacking PTEN are spared from cell death. The proliferation rate of GCPs in
241 *SmoM2* and *SmoM2-Pten*$^{fl/fl}$ mice were similar at P12 (**Fig. 4R**), as determined by injecting EdU
242 1 hour before sacrificing the mice (%EdU+ Ki67+/Ki67+ cells), indicating the latter possibility.
243
244 Given that at P12 the cellular phenotype of GCPs in *SmoM2-Pten*$^{fl/fl}$ mice was similar to in
245 mice at end stage, we analyzed GCPs at P8, eight days after the mice were treated with
246 tamoxifen. Similar to at P12, the area of the proliferating EGL of the cerebellum was significantly
247 greater in both the *SmoM2-Pten*$^{fl/fl}$ and the *SmoM2-Pten*$^{fl/+}$ mice compared to *SmoM2*, although
248 the area of the cerebellum was similar across genotypes likely due to the relatively small increase
249 in EGL area (~2-fold)(**Fig. 5A-E**). Quantification of the proliferation rate (%GFP+ EdU+/GFP+
250 cells in the outer EGL (oEGL) of lobule 4/5 (L5) containing proliferating cells was slightly but
251 significantly higher in the *SmoM2-Pten*$^{fl/fl}$ and the *SmoM2-Pten*$^{fl/+}$ mice compared to *SmoM2* (**Fig.
252 5F**). Moreover, the percentage of mutant (GFP+) cells that remained in the outer EGL of all the
253 GFP+ cells in L5 (including those that differentiated) was significantly higher in the two *Pten*
254 mutant genotypes (**Fig. 5G**). This result indicates that loss or reduction of *Pten* initially induces a
255 pro-proliferative or progenitor state in *SmoM2*-expressing GCPs. By P12 however, *SmoM2-*
256 *Pten*$^{fl/fl}$ GCP-lineage cells accumulate more in the EGL than do *SmoM2-Pten*$^{fl/+}$ or *SmoM2* GCPs,
257 in part because there is an accumulation of NeuN+/SYP+ granule cell (GC)-like cells, likely due
258 to a survival advantage of these cells. This survival advantage suggests that the rapid growth of

259 tumors in *SmoM2-Pten*$^{fl/fl}$ mice is due to accumulation of GC-like cells and would account for the
260 highly differentiated cytology of end stage tumors.
261
262 **Loss of *Pten* in normal GCPs causes increased proliferation and decreased differentiation**
263 Given that *Pten* loss initially increases proliferation and a progenitor state of *SmoM2* (SHH
264 activated) GCPs, we asked whether *Pten* loss in normal GCPs has the same effect. Using our
265 mosaic MASTR approach, we used *Atoh1-FlpoER* to induce GFPcre in scattered GCPs at P0,
266 with or without concomitant deletion of both floxed copies of *Pten* (**Fig. 6A**). As in *SmoM2* GCPs,
267 we found that at P8 a small but significant increase in the proliferation rate and in the proportion
268 of GFP+ cells that remained in the proliferative outer EGL of *Pten* mutant GCPs (**Fig. 6 B-E**).
269 Using *Atoh1-Cre* to delete *Pten* in all GCPs in the embryo (E14 onwards), we found that the
270 cerebellar area of *Atoh1-Pten* conditional mutants (*Atoh1/*+; *Pten*$^{fl/fl}$) was significantly increased
271 at P5 and later, but not at P1 compared to *Atoh1/*+; *Pten*$^{fl/+}$ control mice (**Fig. 6F-N**). Thus, PTEN
272 normally constrains GCP proliferation and possibly differentiation.
273
274 **Loss of *Pten* in *SmoM2* SHH-MB tumor cells results in a cell nonautonomous decrease in**
275 **macrophage infiltration**
276 Given the low density of dying cells in *SmoM2-Pten*$^{fl/fl}$ SHH-MB, we asked whether the tumors
277 have a change in the density of infiltrating macrophages. We previously showed that tumors in
278 *SmoM2* mice have a high infiltration of macrophages ant that they are pro-tumorigenic in a
279 majority of tumors, because reduction of macrophages using PLX5622 treatment leads to a
280 decrease in tumor incidence[27]. Staining of cerebellar tumor sections from *SmoM2-Pten*$^{fl/fl}$ and
281 *SmoM2* mice at end stage revealed the expected high infiltration of IBA1+ macrophages in
282 *SmoM2* tumors, but also a striking decrease in macrophage density in tumors lacking *Pten* (**Fig.**
283 **7A-D**). Moreover, co-staining with Ki67 or NeuN showed that in *SmoM2-Pten*$^{fl/fl}$ mice the
284 macrophages were preferentially located in the areas with proliferating cells and thus increased
285 cell death (**Fig. 7C-F**). The decrease in macrophages in the differentiated regions of *SmoM2-*
286 *Pten*$^{fl/fl}$ mice is not due to a lack of blood vessels, based on CD31 staining of tumors (**Fig. 7G, H**).
287 At P12, in small lesions the macrophages mainly accumulated in the meninges between the
288 lobules but in large lesions they were more concentrated in regions of proliferation in both
289 genotypes and as in end stage were decreased in NeuN+ regions in *SmoM2-Pten*$^{fl/fl}$ mice (**Fig.**
290 **7I-P**). Thus, loss of *Pten* specifically in tumor cells leads to a cell nonautonomous decrease in
291 macrophages in the tumor microenvironment from an early satge.
292

293 **scRNA-seq analysis reveals altered neural differentiation and suppression of immune**
294 **signaling in tumor cells lacking *Pten***
295 To gain insight into transcriptional changes that occur in *SmoM2* SHH-MB tumor cells that lack
296 *Pten* and that could account for the cell autonomous changes seen in the tumors, we performed
297 single cell scRNA-seq of whole tumors dissected from *SmoM2* and *SmoM2-Pten*$^{fl/fl}$ mice (n = 2
298 per genotype). We chose to analyze SHH-MBs from P16 *SmoM2-Pten*$^{fl/fl}$ mice, since this is a few
299 days before mice show signs of disease, and waited until P22 for *SmoM2* mice when the tumors
300 are more visible. Marker analysis of sections of the tumors at the two ages confirmed that the
301 cellular phenotypes of large tumors in *SmoM2-Pten*$^{fl/fl}$ and *SmoM2* mice were similar to tumors at
302 end stage (**Fig. 8–figure supplement 1**). The *SmoM2-Pten*$^{fl/fl}$ tumors had extensive regions of
303 neural differentiation that had reduced cell death (TUNEL particle density) and macrophage
304 density (IBA1+ cells) compared to in proliferative regions (Ki67+) and in *SmoM2* tumors at P22
305 or P16.
306 Tumor cells from the two genotypes separated well in a PCA plot after filtering out poor-
307 quality cells and integrating the replicates (**Fig. 8–figure supplement 2A-C**). Clustering of all
308 cells (17,998 *SmoM2* and 22,864 *SmoM2-Pten*$^{fl/fl}$) was performed[28] to produce twenty clusters
309 with most of the cells, as expected, expressing the GCP lineage marker *Pax6* (clusters 0-9 and
310 13), with nine additional small clusters that included astrocytes, oligodendrocytes, unipolar brush
311 cells, macrophages, endothelial cells and mesenchymal cells (pericytes and fibroblast-like cells)
312 based on marker gene expression (**Fig. 8A, B, Fig. 8–figure supplement 2D, E**, **Table S1**). The
313 cells from each sample were distributed in all clusters, although the proportions of cells from each
314 genotype varied between clusters (**Fig. 8C, Fig. 8–figure supplement 2F, G**, **Table S2**). Within
315 the *Pax6*+ clusters 0-9, based on marker gene expression and cell cycle phase (**Fig. 8D, E**),
316 clusters 3, 4, 8 were proliferative (Ki67+) and enriched for the GCP markers *Gli1*, *Atoh1* and
317 *Barhl1,* indicating highly proliferative GCP-like tumor cells. Cluster 6 had a mixture of cells in G2/M
318 and G1, indicating cells transioning from a proliferative to differentiated state. Clusters 1, 5, 7 had
319 post mitotic (G1) cells that expressed early GC differentiation markers including *Barhl1* and
320 *Slc17a6*, indicating early GC-like cells. Clusters 0, 2, 9 were also in G1 but expressed the mature
321 GC markers *Slc17a7* and *Syp* (**Fig. 8E**) and had a low proportion of cells expressing *Gfp* (**Fig.**
322 **8E**) and a much higher proportion of cells from *SmoM2* mice than from *SmoM2-Pten*$^{fl/fl}$ (**Fig. 8C,**
323 **F, Fig. 8-figure supplement 2G**) indicating mature GC-like cells. Many of the GC-like cells
324 (clusters 0, 2, 9) were likely wild type GCs from the IGL that would disproportionately contaminate
325 the samples from *SmoM2* mice as the tumors were smaller than in *SmoM2-Pten*$^{fl/fl}$ mice. When
326 only the GC-lineage clusters with extensive *Gfp* expression were considered (1, 3, 4, 5, 6, 7, 8),

327 the proportions of cells from the two genotypes were fairly evenly distributed in all clusters (**Fig.**
328 **8G**)
329 Pseudotime analysis[29, 30] reflecting the differentiation pathway of cells within clusters 0-9
330 with an origin in the GCP-like clusters was consistent with our cell type predictions, showing
331 clusters 0, 2, 9 are most mature and that the trajectory proceeds in order through the transitioning
332 cluster 6, then through the early GC-like clusters 1 and 5 to the mature GC cluster 0 and on to
333 cluster 2 or 9 (**Fig. 8H**). The analysis further indicated that early GC-like cluster 7 has a separate
334 differentiation pathway, possibly indicating that loss of PTEN suppresses full differentiation of the
335 GC-like tumor cells. These results are also consistent with our IHC marker analysis of tumor
336 sections that showed that *SmoM2-Pten*$^{fl/fl}$ tumors have an abundance of GC-like cells expressing
337 NeuN and SYP, and further indicated such cels have in an early GC-like state (clusters 1, 5, 7).
338 We next performed differential expression analyses between *SmoM2* and *SmoM2-Pten*$^{fl/fl}$
339 cells in the GCP-like tumor cell clusters (3, 4, 8) and found 1,011 genes were significantly
340 upregulated and 3,710 were downregulated in the cells lacking *Pten* compared to *SmoM2* cells
341 (adjusted p-value≤0.05, **Fig. 9A, Table S3**). Gene set enrichment analysis (GSEA) of Hallmark
342 terms confirmed mTORC1 signaling is significantly unregulated in *SmoM2-Pten*$^{fl/fl}$ tumors
343 compared to *SmoM2*, as well as terms associated with MYC and E2F targets and unfolded protein
344 response (**Fig. 9B, Fig. 9-figure supplement 1A, Table S4**). Violin plots of expression of
345 mTORC1 genes supported upregulation of MTOR signaling (**Fig. 9C**). As for pathways
346 downregulated in *SmoM2-Pten*$^{fl/fl}$ cells compared to *SmoM2*, 'Interferon alpha response' was
347 greatest, and the list included 'complement' and 'inflammatory response' (**Fig. 9D**), possibly
348 contributing to the observed decrease in infiltrating macrophages in such tumors compared to
349 *SmoM2*. Violin plots of genes involved in Interferon alpha signaling supported their down rgulation
350 in tumor cells lacking *Pten* (**Fig. 9E**). GSEA of Gene ontology (GO) terms (biological processes)
351 showed upregulation of terms associated with neural development in *SmoM2-Pten*$^{fl/fl}$ tumors
352 compared to *SmoM2* (**Fig. 9F**, **Fig. 9-figure supplement 1B, Table S5**), indicating loss of PTEN
353 pushes GCP-like cells toward neural differentiation. Violin plots of expression of genes involved
354 in neural regulation supported uprgulation of neurogenesis (**Fig. 9G**).
355
356 **scRNA-seq analysis confirms reduced cell death in differentiated cells of *SmoM2-Pten*$^{fl/fl}$**
357 **tumors**
358 Since our immunohistochemical analysis of *SmoM2-Pten*$^{fl/fl}$ tumors showed that cell death was
359 reduced in the NeuN+/SYP+ regions of tumors, we next performed differential expression
360 analyses of only the *Pten* mutant cells in the early GC-like cluster 1 to the GCP-like clusters 3, 4

361 and 8 and found 2,738 genes were significantly upregulated and 4,185 were downregulated in
362 cluster 1 cells compared to GCP-like cells (adjusted p-value≤0.05, **Fig. 9H, Table S6**). GSEA of
363 GO terms (biological processes) confirmed upregulation of terms associated with neural
364 differentiation and also highlighted down regulation of 'positive regulation of programmed cell
365 death' in *Pten* mutant cells in cluster 1 compared to the GCP-like clusters (**Fig. 9I, K**, **Fig. 9-figure**
366 **supplement 1C, Table S7**). Violin plots of genes underlying the terms supported their altered
367 expression in *SmoM2-Pten*$^{fl/fl}$ tumors compared to *SmoM2* (**Fig. 9J, L**).
368 RNA in situ analysis of sections of P22 *SmoM2* and P16 *SmoM2-Pten*$^{fl/fl}$ tumors was used
369 to confirm some of the genes shown to be differentially expressed between the GCP-like cells in
370 the two genotypes (**Fig. 9M-R**). *Asns* (Unfolded protein gene), *Vldlr* and *Cdkn1a* (mTORC1
371 pathway) showed upregulation in GCP-like tumor cells in P16 *SmoM2-Pten*$^{fl/fl}$ compared to P22
372 *SmoM2* tumors.
373
374 **scRNA-seq analysis indicates loss of *Pten* in *SmoM2* SHH-MB tumor cells results in**
375 **decreased expression of genes associated with cytotoxicity in macrophages**
376 Comparison of the transcriptomes of macrophages in *SmoM2-Pten*$^{fl/fl}$ and *SmoM2* tumors
377 indicated an anti-inflammatory phenotype in tumors lacking *Pten* because genes related to
378 synaptic signaling and *Irf2* were decreased and *Cd36*, a marker of protumoral M2-type
379 macrophages, was upregulated in *SmoM2-Pten*$^{fl/fl}$ tumors (**Fig. 9-figure supplement 1D, E,**
380 **Table S8, S9**)[31, 32]. The observed reduction in macrophage infiltration into *SmoM2-Pten*$^{fl/fl}$ tumors
381 compared to *SmoM2* tumors and the apparent reduction in cytotoxicity might reflect an
382 immunosuppressive tumor microenviroment that could contribute to the rapid growth of tumors
383 lacking PTEN.
384
385 ## Discussion
386 Our work delineates cellular and transcriptional changes that lead to greatly accellerated tumor
387 growth when *Pten* is mosaicly removed in GCPs that have activated SHH-signaling due to
388 expression of SmoM2. We uncovered that in both wild type and *SmoM2* GCPs loss of *Pten* results
389 in an initial increase in mitotic rate and likelihood to remain in the progenitor state. As *SmoM2*
390 tumor formation proceeds, tumors lacking *Pten* accumulate differentiated early GC-like cells that
391 are stalled in their differentiation and are protected from cell death. Thus, the bulk of the *Pten*
392 mutant tumors are post mitotic cells. Macrophages seem to avoid or do not readily penetrate the
393 differentiated regions of the tumors, perhaps because there are less dying cells. With possible
394 relevance to human tumors, unlike previous models of *Pten* heterozygous mutant mice that model

395 Cowden Syndrome or hamartoma syndromes[33] or ones that involve embryonic conditional loss
396 of *Pten* in all GCPs[12, 13], we found that heterozygous loss of *Pten* in sporadic GCPs does not result
397 in more aggressive tumors than activating SHH-siganling alone in rare GCPs. Since our model
398 more closely reflects the sporadic nature of human tumor mutations, our results predict that
399 heterozygous loss of *PTEN* will primarily have a negative impact on disease outcome when the
400 mutations are germline (*PTEN*$^{+/-}$). If human *PTEN* mutant SHH-MB have a similar differentiated
401 cellular phenotype to mouse models, then targeting such tumors with drugs to kill proliferating
402 cells will not remove the bulk of the tumor and will require the drugs having access to the rare
403 proliferating GCP-like tumor stem-like cells.

404 We found that loss or reduction of *Pten* in *SmoM2* mice initially increases expansion of
405 proliferating GCPs through increased proliferation and decreased differentiation such that by P8
406 (one week after gene mutation at P0) the EGL is expanded in *SmoM2-Pten*$^{fl/+}$ and *SmoM2-Pten*$^{fl/fl}$
407 mice compared to *SmoM2*. By P12, however the EGL expansion is greatly exhanced only in
408 *SmoM2-Pten*$^{fl/fl}$ mice, and this is accompanied by an abundance of differentiated cells and a
409 significant reduction in cell death. Our label retention assay involving BrdU injection at P10
410 revealed that a greater proportion of BrdU^{+} *SmoM2-Pten*$^{fl/fl}$ GCPs were Ki67^{-} at P12 than in
411 *SmoM2* mice. This result indicates either that by P10 the loss of *Pten* results in an increase in
412 differentiation of GCPs compared to in *SmoM2* mice, which would be consistent with our scRNA-
413 seq analysis, but also likely due to a greater survival of the differentiated cells since the density
414 of TUNEL^{+} particles is reduced in the EGL of *SmoM2-Pten*$^{fl/fl}$ mice at P12. Consistent with this, it
415 was shown that NeuN+ cells in SHH-MB tumors preferentially die compared to proliferating or
416 quiescent tumor cells in a *Ptch1* mutant model[26]. This previous result is the opposite to what we
417 observed in late stage *SmoM2-Pten*$^{fl/fl}$ tumors where the proliferative comparments of the tumors
418 has greater cell death than the NeuN^{+} or SYP^{+} regions, and a similar density of TUNEL particles
419 to in *SmoM2* tumors. Thus, a key reason for the accelerated tumor growth in *Pten* mutant SHH-
420 MB models is the survival of the differentiated compartment.

421 In a mouse *NeuroD2-SmoA1* model of SHH-MB *Pten* heterozygosity leads to earlier onset
422 of disease and a differentiated/nodular cellular phenotype when *Pten* is deleted in the germline
423 or conditionally throughout the brain (*Nestin-Cre*)[12]. Heterozygous loss of *Pten* in GCPs using an
424 *Atoh1-Cre* transgene to delete *Pten*$^{fl/+}$ and *Ptch1*$^{fl/fl}$ apparently also slightly increases the time of
425 onset and produces a differentiated phenotype[13]. In contrast, in our sporadic SHH-MB model
426 (*SmoM2-Pten*$^{fl/+}$) where only rare GCPs lack one copy of *Pten* (and express *SmoM2*), the time of
427 onset and penetrance are not accelerated and the tumors have a classic histology. Only in rare
428 *SmoM2-Pten*$^{fl/+}$ clones of cells in a minority of tumors where PTEN protein is lacking, likely due to

429 loss of heterozygosity, did we observe a differentiated phenotype with reduced cell death as seen
430 in *SmoM2-Pten*$^{fl/fl}$ mice. The difference in the outcome of our model and the other two is either
431 because of the SHH-activating mutations (SmoM2 vs SmoA1 expression or *Ptch1* loss) or more
432 likely because when all GCPs lack a copy of *Pten* and have activated SHH-signaling that the
433 microenvironemnt provides an advantage for *Pten* heterozygous cells to form a differentiated
434 tumor. It is also possible that another cell type targeted by the other two *Cre* transgenes (*Netstin*
435 and *Atoh1*) supports tumor growth when *Pten* loss is heterozygous.
436 A previous study provided evidence that increased mTOR signaling in SHH-MB promotes
437 spinal cord metastasis by expressing *Shh* in GCPs along with an activated form of AKT[18, 19].
438 However, in our sporadic model and the two other models of *Pten* loss in mouse SHH-MB[12, 13],
439 spinal cord metastasis is not increased. Thus it appears that the way in which the mTOR pathway
440 is activates affects metastasis. Perhaps related to this, in a model of *Trp53* heterozygous loss
441 and *Rictor* homozygous loss, which reduces pAKT, GCPs were found to persist longer than
442 normal in the EGL[34], which is the same as what we found when *Pten* was deleted. Thus, the way
443 the pathway downstream of PTEN is altered disctates the subsequent behavior of the mutant
444 GCPs.
445 In our previous study we showed that in *Kmt2d* mutant SHH-MB models, no difference in
446 tumor size was detected at P12 but by P21 tumors lacking one or two copies of *Kmt2d* were more
447 than twice the size of those with intact *Kmt2d* and had a classic cytoarchitecture. Thus, there is a
448 delayed positive effect of reducing/ablating this chromatin modifier gene on tumor growth rate
449 compared to loss of *Pten* where there is a rapid expansion of the EGL. Another major difference
450 between secondary loss of the two tumor suppressors in SHH-MB is that *Kmt2d* mutant tumors
451 have nearly fully penetrant spinal cord metastasis. Thus, continued mechanistic studies in mouse
452 models of recurrent mutations seen in SHH-MB should provide valuable insights into how the
453 disease is expected to progress and provide ideas for development of targeted therapies based
454 on the cellular phenotypes of tumors not just the signaling pathways altered.
455
456
457 ## Materials and methods
458 **See Key Resources Table (Excel file)**
459 **Animals**
460 The animal care and procedures were performed in accordance with the Memorial Sloan
461 Kettering Cancer Center Institutional Animal Care and Use Committee guidelines (IACUC
462 protocol: 07-01-001). Mice were kept on a 12/12 hour light/dark cycle and in temperature- and

463 humidity-controlled rooms with *ad libitum* access to standard laboratory mouse chow and water.
464 All transgenic mouse lines were maintained on a mixed genetic background containing 129,
465 C57BL/6J, and Swiss Webster. Both sexes were used for the analysis. The following mouse
466 lines were used in the study: *Atoh1-Cre* (JAX #011104), *R26*$^{LSL\text{-}eGFPcre}$ (MASTR, JAX #018903)[22],
467 *Atoh1-FlpoER* (JAX #040091)[23], *Pten*$^{fl/fl}$ [25] and *SmoM2* (#005130)[24]. Genetic recombination was
468 induced with FlpoER by injecting one 100µg/g dose of Tamoxifen (Tm) (Sigma-Aldrich)
469 subcutaneously into the back of P0 mice. Tm was prepared in corn oil (Sigma-Aldrich) at 20
470 mg/mL and stored at 4°C.

471 **Tissue preparation**

472 For all histological analyses, mice were anesthetized with isoflurane and then perfused
473 transcardially with room temperature (RT) phosphate buffered saline (PBS) with heparin (0.02
474 mg/mL) and then ice cold 4% paraformaldehyde (PFA, Electron Microscopy Sciences, catalog
475 no: 15714). Brains and spinal cords were dissected and post-fixed in 4% PFA 3-4 days at 4°C
476 and cryopreserved in 30% sucrose in PBS for ~2 days at 4°C. Brains were embedded in Tissue-
477 Tek OCT compound (Sakura Finetek). Brains were serially cryosectioned sagittally at 12 µm and
478 collected on charged glass slides (Fisherbrand ColorFrost Plus) and stored at -20°C. Frozen
479 spinal cords were coronally sectioned at 20um. Details of reagents are listed in **Key Resources**
480 **Table**.

481 **Hematoxylin and eosin (H&E) staining**

482 H&E staining were obtained from Richard-Allan Scientific and includ hematoxylin 2 solution,
483 eosin-Y, bluing reagent, and clarifier 2. Slides were rinsed in PBS for 5 min and incubated in
484 hematoxylin 2 solution for 3 min and then rinsed in deionized water (diH_2O) and placed in staining
485 reagents for 1 min each (diH_2O, clarifier 2, diH_2O, bluing reagent , diH_2O, eosin-Y). Dehydration
486 and defatting were then performed (dH_2O-70% ethanol-95%–95%-100%-100%-xylene-xylene-
487 xylene, 1 min each) and thenslides were mounted with a coverslip and DPX mounting medium
488 (Electron Microscopy Sciences). Details of reagents are listed in **Key Resources Table**.

489 **Immunofluorescence**

490 Slides were washed 3 time for 5 min in PBS. When necessary, antigen retrieval was then
491 performed by immersing slides in sodium citrate buffer (10 mM sodium citrate with 0.05% Tween-
492 20, pH 6.0) for 20 min at 95°C followed by rinsing in PBS. Slides were then incubated in blocking
493 buffer (5% BSA in 0.4% Triton-X100 in PBS (PBST)) for 1 hour at RT. Slides were then placed in
494 primary antibody solution in blocking buffer at 4°C overnight. Primary antibody information and
495 dilutions are listed in **Key Resources Tables**. Slides were then rinsed three times in RT 0.1%
496 PBST and incubated in secondary antibody solution in blocking buffer (1:500) at RT for 1 hour.

497 Slides then were incubated in Hoechst (Invitrogen, catalog #H3569 diluted 1:1000 in PBS) for 10
498 min and rinsed three times in PBS and cover-slipped with Fluoro-Gel (Electron Microscopy
499 Sciences).

500 **TUNEL Staining**

501 TUNEL staining was according to th manufacturers instructions (Roche TUNEL assay kit). Tissue
502 on slides were permeabilized with 0.5% TritonX-100 and then pre-incubated with 1x TdT reaction
503 buffer with 5mM $CoCl_2$ and 1X PBS for 15 min at RT. Slides were then incubated for 1 hr at 37°C
504 in 1x TdT reaction buffer containing Terminal Transferase (Roche) and Biotin-16-dUTP (Sigma-
505 Aldrich) or Digoxigenin-dUTP (Enzo Life Sciences, Inc). Slides were then incubated with a
506 Streptavidin Alexa Fluor 647 conjugate (Invitrogen catalog #S-32357) or Anti-Digoxigenin-
507 Rhodamine (Sigma-Aldrich catalog), respectively for 1 hr.

508 **BrdU Injection and Staining**

509 To assess cell differentiation, BrdU (Sigma Aldrich) was injected intraperitoneally at 50 µg/g at
510 P10 for analysis at P12. Tissues were collected and processed as described above. For
511 immunostaining, antigen retrival was applied to slides with Rat primary anti-BrdU antibody BU1/75
512 (ICR1) (Abcam Inc.) to detect BrdU.

513 **EdU (5-ethynyl-2'-deoxyuridine) Injection and Staining**

514 To assess cell proliferation, EdU (Invitrogen) was injected intraperitoneally at 50 µg/g 1 hr before
515 euthanasia. A Click-it EdU assay was used (Invitrogen) with Sulfo-Cyanine5 azide (Lumiprobe
516 Corporation) per the manufacturer's protocol to stain sections.

517 **RNA *in situ* hybridization**

518 Sagittal sections (12 um) were processed for *in situ* hybridization as described[35]. Except for *Gli1*
519 and *Syp,* antisense riboprobes were labeled with UTP-digoxigenin using a DIG RNA labeling mix
520 (Sigma-Aldrich) with PCR-amplified templates prepared from cDNA synthesized from an early
521 postnatal mouse cerebellum lysate. Signal was detected with alkaline phosphatase-coupled anti-
522 digoxigenin antibodies using BM purple (Sigma-Aldrich) as the substrate. The primers used for
523 PCR amplification were based on the Allen Brain Atlas. *Gli1* RNA in situ was performed using an
524 antisense RNA probe made from a plasmid[31] and for *Syp* BioMatik generanted a plasmid in
525 Bluescript containing *Syp* sequences using the primers described in the **Key Resources Tables.**
526 Primers were flanked in the 3' with SP6 (antisense) and 5' with T3 (sense) promoters. Primers for
527 RNA in situ probes are listed in **Key Resources Tables**.

528 **Microscopy, image processing, and analyses**

529 Images were acquired with a DM6000 Leica fluorescent microscope (Leica Camera, Wetzlar,
530 Germany) or NanoZoomer Digital Pathology microscope (Hamamatsu Photonics, Shizuoka,

531 Japan) and were processed and analyzed using Fiji[36] or Photoshop (Adobe Inc., San Jose, CA,
532 USA). Cell counts were manually obtained using the Cell Counter plugin for Fiji or semi-automated
533 using a custom script using the Analyze Particle plugin for Fiji as previously described[37].

534 **ScRNA-seq sample Preparation**

535 *Atoh1-FlpoER/+*; *R26*$^{MASTR/LSL\text{-}SmoM2}$;*Pten*$^{+/+}$ (SmoM2) and *Atoh1-FlpoER/+*; *R26*$^{MASTR/LSL\text{-}SmoM2}$;
536 *Pten*$^{fl/fl}$ (*SmoM2 Pten*$^{fl/fl}$) mice were euthanized at P16 and P22, respectively, and the tumors were
537 dissected from the lateral-posterior cerebellum in ice-cold Hank's balanced salt solution (HBSS,
538 Gibco). Then the tumors were dissociated in Papain (Worthington) for 30 minutes at 37°C before
539 being washed out in Ovalbumin (Worthington). Tumors were triturated by pipetting up and down
540 using a P1000 and filtered through a 40µm cell strainer (Falcon). Once the cells were dissociated,
541 the dead cells were removed using the kit EasySep Dead Cell Removal (Annexin V) (StemCell).
542 Then cells were centrifuged at 500g at 4°C for 5 minutes. Cells were then washed with PBS. For
543 every sample (2 *SmoM2* and 2 *SmoM2 Pten*$^{fl/fl}$), cells were counted using 0.2% Trypan on
544 hemocytometer and diluted before loading to 10X chip, targeting 10,000 viable cells per sample.
545 The scRNA-Seq of tumor cell suspensions was performed on a Chromium instrument (10X
546 genomics) following the user guide manual for 3' v3.1. Final libraries were sequenced on an
547 Illumina NovaSeq6000 by the IGO core of MSKCC.

548 **scRNA-seq data analysis**

549 The Cell Ranger Single Cell software suite (10x Genomics) was used to align reads and generate
550 feature-barcode matrices. The reference genome used was the Genome Reference Consortium
551 Mouse Build 38 (GRCm38, Gencode annotation mm10). Raw reads were processed using the
552 Cell Ranger count program using default parameters.
553 Seurat v5.0.2 package was used to generate a UMI (unique molecular identifier) count matrix
554 from the Cell Ranger output[38]. Genes expressed in less than 10 cells were removed for further
555 analyses. Cells with larger than 18000 UMIs, 0.20 mitoRatio, UMI≤500 and ≤500 genes detected
556 were considered low quality/outliers and discarded from the datasets. Normalization was
557 performed on individual samples using the NormalizeData function with default parameters. The
558 normalized data was scaled by ScaleData function with mitochondrial gene percentage regressed
559 out. Principal component analysis (PCA) was performed on the scaled data by runPCA. Samples
560 were then integrated using IntegrateLayers function with the Harmony Integration method. The
561 first 20 dimensions were used for the FindNeighbors function, and clusters were identified using
562 the FindClusters function with a resolution of 0.5. Data were projected onto the 2D space using
563 the FindUMAP or RunUMAP function with 20 dimensions. Cluster markers and further differential
564 gene expression analyses were performed using normalized counts (NormalizeData) in the RNA

assay. Cluster markers were identified using the FindAllMarkers and comparing markers generated to the literature. To refine clustering further, the SubsetData function was used to create a new Seurat object, and the above clustering was reiterated.

Differential gene expression analyses between genotypes or clusters were performed using the FindMarkers function in the Seurat package. Genes with an adjusted *P* value (*Padj*) < 0.05 were considered significantly up or downregulated. Results were visualized by Violin plot and Umap plot using Seurat package, and Volcano plot using the EnhancedVolcano package on Bioconductor[39]. GSEA analysis on GO and Hallmark terms were performed using the enrichGO, clusterProfiler packages on Bioconductor[40]. To build a pseudotime trajectory using the UMAP data, the Seurat object was converted to a monocle 3 (1.3.7) object by as.cell_data_set function[29, 30]. Cells were then clustered by the cluster cells function. The trajectory GCP-lineage partition was constructed using learn graph function followed by order cells function.

Statstic analysis

All statistical analyses to quantify data were performed using Prism software (GraphPad) and significance was determined as P <= 0.05. Each statistical analysis used is described in the figure legends. Data (shown as scatter graphs) were presented as mean±standard deviation.

Acknowledgements

We thank members of the Joyner lab for interesting discussions pertaining to SHH-MB and technical support, in particular Reeti Mayur Sanghrajka for insightful suggestions at the beginning of the study. We thank the Memorial Sloan Kettering Cancer Center Flow Cytometry Core, Integrated Genomics Operations Core Facility and the Center for Comparative Medicine and Pathology for technical support.

Additional Information

Competing interests

All authors declare to have no actual or potential conflict of interest including any financial, personal, or other relationships with other people or organizations within three years of beginning the submitted work that could inappropriately influence, or be perceived to influence, their work.

Funding

NCI (R01CA192176), Alexandra L Joyner

MSK Functional Genomics Initiative (GC242211), Alexandra L Joyner

NCI Cancer Center Support Grant (CCSG, P30 CA08748), Alexandra L Joyner

Cycle for Survival, Alexandra L Joyner

599 ## Ethics

600 No ethical consideration as no human data were analyzed.

601 ## Author contributions

602 Z.L., S.E.N., Y.L and A.L.J. formulated experiments and analysis approaches. Z.L. and D.N.S.
603 performed animal and histological experiments. Z.L. performed section analysis and
604 quantifications. Z.L., S.E.N. and Y.L. performed scRNA-seq analysis. A.L.J. wrote the draft
605 manuscript and Z.L., Y. L., S.E.N. and A.L.J. prepared Figures and edited the manuscript.

606 ## Author ORCIDs

607 Alexandra L Joyner, ORCID ID: 0000-0001-7090-9605, http://orcid.org/0000-0001-7090-9605

608

609 **Additional files**

610 ## Supplementary Tables

611 **Table S1.** Top cell markers for each cluster in merged scRNA-seq data. Related to Figure 8-
612 Supplement 2D, E.

613 **Table S2.** Cell numbers per cluster for each genotype based on merged scRNA-seq data. Related
614 to Figure 8 F, G and Figure 8-Supplement 2G.

615 **Table S3**. scRNA-seq differential gene expression analysis of GCP-like tumor cells comparing
616 SmoM2; Ptenfl/fl to SmoM2. Related to Figure 9A.

617 **Table S4.** GSEA analysis of Hallmark terms of DEG gene list of GCP-like cells in SmoM2; Ptenfl/fl
618 compared with SmoM2 tumors. Related to Figure 9-Supplemental 1A.

619 **Table S5**. GSEA analysis of Gene Ontology terms of DEG gene list of GCP-like cells in SmoM2;
620 Ptenfl/fl compared with SmoM2 tumors. Related to Figure 9-Supplemental 1B.

621 **Table S6**. scRNA-seq differential gene expression analysis in early GC-like (cluster 1) compared
622 with GCP-like (clusters 3, 4, 8) in SmoM2; Ptenfl/fl tumors. Related to Figure 9H.

623 **Table S7**. GSEA analysis of Gene Ontology terms of DEG gene list in early GC-like (cluster 1)
624 compared with GCP-like (clusters 3, 4, 8) of SmoM2; Ptenfl/fl tumors. Related to Figure 9-
625 Supplemental 1C.

626 **Table S8**. scRNA-seq differential gene expression analysis of macrophages in SmoM2; Ptenfl/fl
627 compared with SmoM2 tumors. Related to Figure 9-Supplement 1D.

Table S9. GSEA analysis of Gene Ontology terms of DEG gene list of macrophages in SmoM2; Ptenfl/fl compared with SmoM2 tumors. Related to Figure 9-Supplement 1D.

Key Resources Table

Data Availability

Sequencing data have been deposited in GEO (token czkvuymyhnktrgp) under accession code GSE295733. All experimental data generated and analyzed in this study are included in the manuscript and supporting files.

Referenecs

1. Taylor MD, Northcott PA, Korshunov A, Remke M, Cho YJ, Clifford SC, Eberhart CG, Parsons DW, Rutkowski S, Gajjar A, Ellison DW, Lichter P, Gilbertson RJ, Pomeroy SL, Kool M, Pfister SM. Molecular subgroups of medulloblastoma: the current consensus. Acta Neuropathol. 2012;123(4):465-72. Epub 20111202. doi: 10.1007/s00401-011-0922-z. PubMed PMID: 22134537; PMCID: PMC3306779.

2. Cavalli FMG, Remke M, Rampasek L, Peacock J, Shih DJH, Luu B, Garzia L, Torchia J, Nor C, Morrissy AS, Agnihotri S, Thompson YY, Kuzan-Fischer CM, Farooq H, Isaev K, Daniels C, Cho BK, Kim SK, Wang KC, Lee JY, Grajkowska WA, Perek-Polnik M, Vasiljevic A, Faure-Conter C, Jouvet A, Giannini C, Nageswara Rao AA, Li KKW, Ng HK, Eberhart CG, Pollack IF, Hamilton RL, Gillespie GY, Olson JM, Leary S, Weiss WA, Lach B, Chambless LB, Thompson RC, Cooper MK, Vibhakar R, Hauser P, van Veelen MC, Kros JM, French PJ, Ra YS, Kumabe T, López-Aguilar E, Zitterbart K, Sterba J, Finocchiaro G, Massimino M, Van Meir EG, Osuka S, Shofuda T, Klekner A, Zollo M, Leonard JR, Rubin JB, Jabado N, Albrecht S, Mora J, Van Meter TE, Jung S, Moore AS, Hallahan AR, Chan JA, Tirapelli DPC, Carlotti CG, Fouladi M, Pimentel J, Faria CC, Saad AG, Massimi L, Liau LM, Wheeler H, Nakamura H, Elbabaa SK, Perezpeña-Diazconti M, Chico Ponce de León F, Robinson S, Zapotocky M, Lassaletta A, Huang A, Hawkins CE, Tabori U, Bouffet E, Bartels U, Dirks PB, Rutka JT, Bader GD, Reimand J, Goldenberg A, Ramaswamy V, Taylor MD. Intertumoral Heterogeneity within Medulloblastoma Subgroups. Cancer Cell. 2017;31(6):737-54.e6. doi: 10.1016/j.ccell.2017.05.005. PubMed PMID: 28609654; PMCID: PMC6163053.

3. Kool M, Jones DT, Jäger N, Northcott PA, Pugh TJ, Hovestadt V, Piro RM, Esparza LA, Markant SL, Remke M, Milde T, Bourdeaut F, Ryzhova M, Sturm D, Pfaff E, Stark S, Hutter S, Seker-Cin H, Johann P, Bender S, Schmidt C, Rausch T, Shih D, Reimand J, Sieber L, Wittmann A, Linke L, Witt H, Weber UD, Zapatka M, König R, Beroukhim R, Bergthold G, van Sluis P, Volckmann R, Koster J, Versteeg R, Schmidt S, Wolf S, Lawerenz C, Bartholomae CC, von Kalle C, Unterberg A, Herold-Mende C, Hofer S, Kulozik AE, von Deimling A, Scheurlen W, Felsberg J, Reifenberger G, Hasselblatt M, Crawford JR, Grant GA, Jabado N, Perry A, Cowdrey C, Croul S, Zadeh G, Korbel JO, Doz F, Delattre O, Bader GD, McCabe MG, Collins VP, Kieran MW, Cho YJ, Pomeroy SL, Witt O, Brors B, Taylor MD, Schüller U, Korshunov A, Eils R, Wechsler-Reya RJ, Lichter P, Pfister SM. Genome sequencing of SHH medulloblastoma predicts genotype-

669 related response to smoothened inhibition. Cancer Cell. 2014;25(3):393-405. doi:
670 10.1016/j.ccr.2014.02.004. PubMed PMID: 24651015; PMCID: PMC4493053.

671 4. Robinson GW, Rudneva VA, Buchhalter I, Billups CA, Waszak SM, Smith KS, Bowers DC,
672 Bendel A, Fisher PG, Partap S, Crawford JR, Hassall T, Indelicato DJ, Boop F, Klimo P, Sabin
673 ND, Patay Z, Merchant TE, Stewart CF, Orr BA, Korbel JO, Jones DTW, Sharma T, Lichter P,
674 Kool M, Korshunov A, Pfister SM, Gilbertson RJ, Sanders RP, Onar-Thomas A, Ellison DW, Gajjar
675 A, Northcott PA. Risk-adapted therapy for young children with medulloblastoma (SJYC07):
676 therapeutic and molecular outcomes from a multicentre, phase 2 trial. Lancet Oncol.
677 2018;19(6):768-84. Epub 20180516. doi: 10.1016/s1470-2045(18)30204-3. PubMed PMID:
678 29778738; PMCID: PMC6078206.

679 5. Schwalbe EC, Lindsey JC, Nakjang S, Crosier S, Smith AJ, Hicks D, Rafiee G, Hill RM,
680 Iliasova A, Stone T, Pizer B, Michalski A, Joshi A, Wharton SB, Jacques TS, Bailey S, Williamson
681 D, Clifford SC. Novel molecular subgroups for clinical classification and outcome prediction in
682 childhood medulloblastoma: a cohort study. Lancet Oncol. 2017;18(7):958-71. Epub 20170522.
683 doi: 10.1016/s1470-2045(17)30243-7. PubMed PMID: 28545823; PMCID: PMC5489698.

684 6. Garcia-Lopez J, Kumar R, Smith KS, Northcott PA. Deconstructing Sonic Hedgehog
685 Medulloblastoma: Molecular Subtypes, Drivers, and Beyond. Trends Genet. 2021;37(3):235-50.
686 Epub 20201201. doi: 10.1016/j.tig.2020.11.001. PubMed PMID: 33272592.

687 7. Sanghrajka RM, Koche R, Medrano H, El Nagar S, Stephen DN, Lao Z, Bayin NS, Ge K,
688 Joyner AL. KMT2D suppresses Sonic hedgehog-driven medulloblastoma progression and
689 metastasis. iScience. 2023;26(10):107831. Epub 20230909. doi: 10.1016/j.isci.2023.107831.
690 PubMed PMID: 37822508; PMCID: PMC10562805.

691 8. Lee YR, Chen M, Pandolfi PP. The functions and regulation of the PTEN tumour
692 suppressor: new modes and prospects. Nat Rev Mol Cell Biol. 2018;19(9):547-62. doi:
693 10.1038/s41580-018-0015-0. PubMed PMID: 29858604.

694 9. Hopkins BD, Fine B, Steinbach N, Dendy M, Rapp Z, Shaw J, Pappas K, Yu JS, Hodakoski
695 C, Mense S, Klein J, Pegno S, Sulis ML, Goldstein H, Amendolara B, Lei L, Maurer M, Bruce J,
696 Canoll P, Hibshoosh H, Parsons R. A secreted PTEN phosphatase that enters cells to alter
697 signaling and survival. Science. 2013;341(6144):399-402. Epub 20130606. doi:
698 10.1126/science.1234907. PubMed PMID: 23744781; PMCID: PMC3935617.

699 10. Putz U, Howitt J, Doan A, Goh CP, Low LH, Silke J, Tan SS. The tumor suppressor PTEN
700 is exported in exosomes and has phosphatase activity in recipient cells. Sci Signal.
701 2012;5(243):ra70. Epub 20120925. doi: 10.1126/scisignal.2003084. PubMed PMID: 23012657.

702 11. Zhang C, Ma HM, Wu S, Shen JM, Zhang N, Xu YL, Li CX, He P, Ge MK, Chu XL, Zhang
703 YX, Zheng JK, Chen GQ, Shen SM. Secreted PTEN binds PLXDC2 on macrophages to drive
704 antitumor immunity and tumor suppression. Dev Cell. 2024;59(23):3072-88.e8. Epub 20240827.
705 doi: 10.1016/j.devcel.2024.08.003. PubMed PMID: 39197453.

706 12. Castellino RC, Barwick BG, Schniederjan M, Buss MC, Becher O, Hambardzumyan D,
707 Macdonald TJ, Brat DJ, Durden DL. Heterozygosity for Pten promotes tumorigenesis in a mouse
708 model of medulloblastoma. PLoS One. 2010;5(5):e10849. Epub 20100526. doi:
709 10.1371/journal.pone.0010849. PubMed PMID: 20520772; PMCID: PMC2877103.

710 13. Metcalfe C, Alicke B, Crow A, Lamoureux M, Dijkgraaf GJ, Peale F, Gould SE, de Sauvage
711 FJ. PTEN loss mitigates the response of medulloblastoma to Hedgehog pathway inhibition.
712 Cancer Res. 2013;73(23):7034-42. Epub 20131023. doi: 10.1158/0008-5472.Can-13-1222.
713 PubMed PMID: 24154871.

714 14. Corrales JD, Blaess S, Mahoney EM, Joyner AL. The level of sonic hedgehog signaling
715 regulates the complexity of cerebellar foliation. Development. 2006;133(9):1811-21. Epub
716 20060329. doi: 10.1242/dev.02351. PubMed PMID: 16571625.

717 15. Lewis PM, Gritli-Linde A, Smeyne R, Kottmann A, McMahon AP. Sonic hedgehog
718 signaling is required for expansion of granule neuron precursors and patterning of the mouse
719 cerebellum. Dev Biol. 2004;270(2):393-410. doi: 10.1016/j.ydbio.2004.03.007. PubMed PMID:
720 15183722.

721 16. Joyner AL, Bayin NS. Cerebellum lineage allocation, morphogenesis and repair: impact
722 of interplay amongst cells. Development. 2022;149(18). Epub 20220929. doi:
723 10.1242/dev.185587. PubMed PMID: 36172987; PMCID: PMC9641654.

724 17. Tronche F, Kellendonk C, Kretz O, Gass P, Anlag K, Orban PC, Bock R, Klein R, Schütz
725 G. Disruption of the glucocorticoid receptor gene in the nervous system results in reduced anxiety.
726 Nat Genet. 1999;23(1):99-103. doi: 10.1038/12703. PubMed PMID: 10471508.

727 18. Wu X, Northcott PA, Dubuc A, Dupuy AJ, Shih DJ, Witt H, Croul S, Bouffet E, Fults DW,
728 Eberhart CG, Garzia L, Van Meter T, Zagzag D, Jabado N, Schwartzentruber J, Majewski J,
729 Scheetz TE, Pfister SM, Korshunov A, Li XN, Scherer SW, Cho YJ, Akagi K, MacDonald TJ,
730 Koster J, McCabe MG, Sarver AL, Collins VP, Weiss WA, Largaespada DA, Collier LS, Taylor
731 MD. Clonal selection drives genetic divergence of metastatic medulloblastoma. Nature.
732 2012;482(7386):529-33. Epub 20120215. doi: 10.1038/nature10825. PubMed PMID: 22343890;
733 PMCID: PMC3288636.

734 19. Mumert M, Dubuc A, Wu X, Northcott PA, Chin SS, Pedone CA, Taylor MD, Fults DW.
735 Functional genomics identifies drivers of medulloblastoma dissemination. Cancer Res.
736 2012;72(19):4944-53. Epub 20120808. doi: 10.1158/0008-5472.Can-12-1629. PubMed PMID:
737 22875024; PMCID: PMC3463769.

738 20. Gao J, Aksoy BA, Dogrusoz U, Dresdner G, Gross B, Sumer SO, Sun Y, Jacobsen A,
739 Sinha R, Larsson E, Cerami E, Sander C, Schultz N. Integrative analysis of complex cancer
740 genomics and clinical profiles using the cBioPortal. Sci Signal. 2013;6(269):pl1. Epub 20130402.
741 doi: 10.1126/scisignal.2004088. PubMed PMID: 23550210; PMCID: PMC4160307.

742 21. Cerami E, Gao J, Dogrusoz U, Gross BE, Sumer SO, Aksoy BA, Jacobsen A, Byrne CJ,
743 Heuer ML, Larsson E, Antipin Y, Reva B, Goldberg AP, Sander C, Schultz N. The cBio cancer
744 genomics portal: an open platform for exploring multidimensional cancer genomics data. Cancer
745 Discov. 2012;2(5):401-4. doi: 10.1158/2159-8290.Cd-12-0095. PubMed PMID: 22588877;
746 PMCID: PMC3956037.

747 22. Lao Z, Raju GP, Bai CB, Joyner AL. MASTR: a technique for mosaic mutant analysis with
748 spatial and temporal control of recombination using conditional floxed alleles in mice. Cell Rep.
749 2012;2(2):386-96. Epub 20120809. doi: 10.1016/j.celrep.2012.07.004. PubMed PMID:
750 22884371; PMCID: PMC3460375.

751 23. Tan IL, Wojcinski A, Rallapalli H, Lao Z, Sanghrajka RM, Stephen D, Volkova E,
752 Korshunov A, Remke M, Taylor MD, Turnbull DH, Joyner AL. Lateral cerebellum is preferentially
753 sensitive to high sonic hedgehog signaling and medulloblastoma formation. Proc Natl Acad Sci U
754 S A. 2018;115(13):3392-7. Epub 20180312. doi: 10.1073/pnas.1717815115. PubMed PMID:
755 29531057; PMCID: PMC5879676.

756 24. Mao J, Ligon KL, Rakhlin EY, Thayer SP, Bronson RT, Rowitch D, McMahon AP. A novel
757 somatic mouse model to survey tumorigenic potential applied to the Hedgehog pathway. Cancer
758 Res. 2006;66(20):10171-8. doi: 10.1158/0008-5472.Can-06-0657. PubMed PMID: 17047082;
759 PMCID: PMC3806052.

760 25. Trotman LC, Niki M, Dotan ZA, Koutcher JA, Di Cristofano A, Xiao A, Khoo AS, Roy-
761 Burman P, Greenberg NM, Van Dyke T, Cordon-Cardo C, Pandolfi PP. Pten dose dictates cancer
762 progression in the prostate. PLoS Biol. 2003;1(3):E59. Epub 20031027. doi:
763 10.1371/journal.pbio.0000059. PubMed PMID: 14691534; PMCID: PMC270016.

764 26. Vanner RJ, Remke M, Gallo M, Selvadurai HJ, Coutinho F, Lee L, Kushida M, Head R,
765 Morrissy S, Zhu X, Aviv T, Voisin V, Clarke ID, Li Y, Mungall AJ, Moore RA, Ma Y, Jones SJ,
766 Marra MA, Malkin D, Northcott PA, Kool M, Pfister SM, Bader G, Hochedlinger K, Korshunov A,
767 Taylor MD, Dirks PB. Quiescent sox2(+) cells drive hierarchical growth and relapse in sonic
768 hedgehog subgroup medulloblastoma. Cancer Cell. 2014;26(1):33-47. Epub 20140619. doi:
769 10.1016/j.ccr.2014.05.005. PubMed PMID: 24954133; PMCID: PMC4441014.

770 27. Tan IL, Arifa RDN, Rallapalli H, Kana V, Lao Z, Sanghrajka RM, Sumru Bayin N, Tanne
771 A, Wojcinski A, Korshunov A, Bhardwaj N, Merad M, Turnbull DH, Lafaille JJ, Joyner AL. CSF1R
772 inhibition depletes tumor-associated macrophages and attenuates tumor progression in a mouse
773 sonic Hedgehog-Medulloblastoma model. Oncogene. 2021;40(2):396-407. Epub 20201106. doi:
774 10.1038/s41388-020-01536-0. PubMed PMID: 33159168; PMCID: PMC7855734.

775 28. Hao Y, Hao S, Andersen-Nissen E, Mauck WM, 3rd, Zheng S, Butler A, Lee MJ, Wilk AJ,
776 Darby C, Zager M, Hoffman P, Stoeckius M, Papalexi E, Mimitou EP, Jain J, Srivastava A, Stuart
777 T, Fleming LM, Yeung B, Rogers AJ, McElrath JM, Blish CA, Gottardo R, Smibert P, Satija R.
778 Integrated analysis of multimodal single-cell data. Cell. 2021;184(13):3573-87.e29. Epub
779 20210531. doi: 10.1016/j.cell.2021.04.048. PubMed PMID: 34062119; PMCID: PMC8238499.

780 29. Trapnell C, Cacchiarelli D, Grimsby J, Pokharel P, Li S, Morse M, Lennon NJ, Livak KJ,
781 Mikkelsen TS, Rinn JL. The dynamics and regulators of cell fate decisions are revealed by
782 pseudotemporal ordering of single cells. Nat Biotechnol. 2014;32(4):381-6. Epub 20140323. doi:
783 10.1038/nbt.2859. PubMed PMID: 24658644; PMCID: PMC4122333.

784 30. Qiu X, Mao Q, Tang Y, Wang L, Chawla R, Pliner HA, Trapnell C. Reversed graph
785 embedding resolves complex single-cell trajectories. Nat Methods. 2017;14(10):979-82. Epub
786 20170821. doi: 10.1038/nmeth.4402. PubMed PMID: 28825705; PMCID: PMC5764547.

787 31. Qin RX, Ma XY, Han ZY, Ma SY, Shen ZJ, Lu ZH, Sun Y, Yu WL. IRF2 Affects LPS- and
788 IFN-γ-Induced Pro-Inflammatory Responses, Cell Viability, Migration and Apoptosis of
789 Macrophages by Regulating IRG1. J Inflamm Res. 2024;17:9651-64. Epub 20241125. doi:
790 10.2147/jir.S490655. PubMed PMID: 39618923; PMCID: PMC11606192.

791 32. Yang P, Qin H, Li Y, Xiao A, Zheng E, Zeng H, Su C, Luo X, Lu Q, Liao M, Zhao L, Wei L,
792 Varghese Z, Moorhead JF, Chen Y, Ruan XZ. CD36-mediated metabolic crosstalk between tumor

cells and macrophages affects liver metastasis. Nat Commun. 2022;13(1):5782. Epub 20221002. doi: 10.1038/s41467-022-33349-y. PubMed PMID: 36184646; PMCID: PMC9527239.

33. Blumenthal GM, Dennis PA. PTEN hamartoma tumor syndromes. Eur J Hum Genet. 2008;16(11):1289-300. Epub 20080910. doi: 10.1038/ejhg.2008.162. PubMed PMID: 18781191; PMCID: PMC6939673.

34. Akgül S, Li Y, Zheng S, Kool M, Treisman DM, Li C, Wang Y, Gröbner S, Ikenoue T, Shen Y, Camelo-Piragua S, Tomasek G, Stark S, Guduguntla V, Gusella JF, Guan KL, Pfister SM, Verhaak RGW, Zhu Y. Opposing Tumor-Promoting and -Suppressive Functions of Rictor/mTORC2 Signaling in Adult Glioma and Pediatric SHH Medulloblastoma. Cell Rep. 2018;24(2):463-78.e5. doi: 10.1016/j.celrep.2018.06.050. PubMed PMID: 29996106; PMCID: PMC6116735.

35. Blaess S, Bodea GO, Kabanova A, Chanet S, Mugniery E, Derouiche A, Stephen D, Joyner AL. Temporal-spatial changes in Sonic Hedgehog expression and signaling reveal different potentials of ventral mesencephalic progenitors to populate distinct ventral midbrain nuclei. Neural Dev. 2011;6:29. Epub 20110620. doi: 10.1186/1749-8104-6-29. PubMed PMID: 21689430; PMCID: PMC3135491.

36. Schindelin J, Arganda-Carreras I, Frise E, Kaynig V, Longair M, Pietzsch T, Preibisch S, Rueden C, Saalfeld S, Schmid B, Tinevez JY, White DJ, Hartenstein V, Eliceiri K, Tomancak P, Cardona A. Fiji: an open-source platform for biological-image analysis. Nat Methods. 2012;9(7):676-82. Epub 20120628. doi: 10.1038/nmeth.2019. PubMed PMID: 22743772; PMCID: PMC3855844.

37. Willett RT, Bayin NS, Lee AS, Krishnamurthy A, Wojcinski A, Lao Z, Stephen D, Rosello-Diez A, Dauber-Decker KL, Orvis GD, Wu Z, Tessier-Lavigne M, Joyner AL. Cerebellar nuclei excitatory neurons regulate developmental scaling of presynaptic Purkinje cell number and organ growth. Elife. 2019;8. Epub 20191119. doi: 10.7554/eLife.50617. PubMed PMID: 31742552; PMCID: PMC6890462.

38. Satija R, Farrell JA, Gennert D, Schier AF, Regev A. Spatial reconstruction of single-cell gene expression data. Nat Biotechnol. 2015;33(5):495-502. Epub 20150413. doi: 10.1038/nbt.3192. PubMed PMID: 25867923; PMCID: PMC4430369.

39. Blighe K, Rana S, Lewis M. EnhancedVolcano: Publication-ready volcano plots with enhanced colouring and labeling. R package version 1260. 2025. doi: doi:10.18129/B9.bioc.EnhancedVolcano.

40. Yu G, Wang LG, Han Y, He QY. clusterProfiler: an R package for comparing biological themes among gene clusters. Omics. 2012;16(5):284-7. Epub 20120328. doi: 10.1089/omi.2011.0118. PubMed PMID: 22455463; PMCID: PMC3339379.

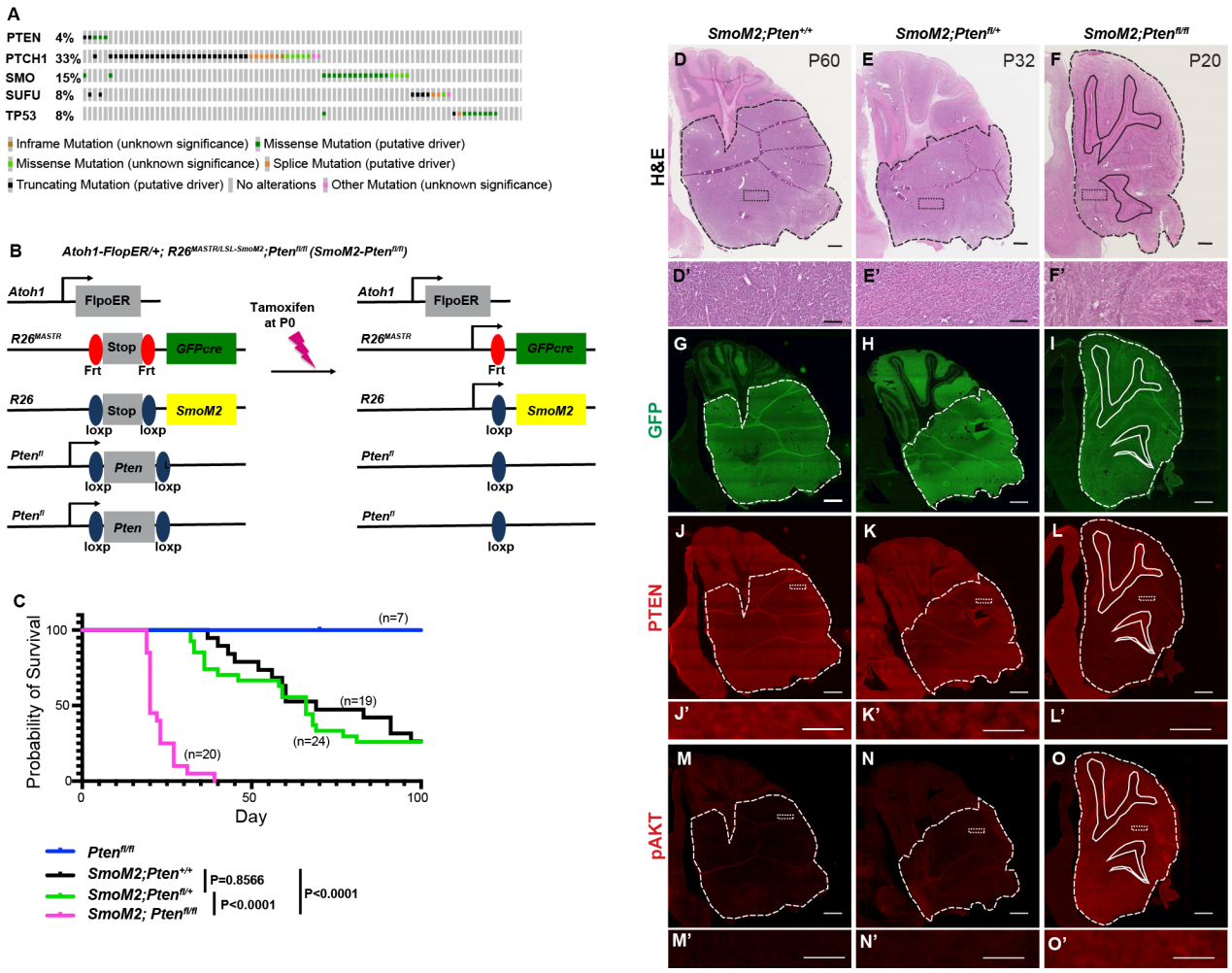

Figure 1. **Homozygous but not heterozygous loss of *Pten* in a sporadic mouse model of *SmoM2* SHH-MB increases penetrance and reduces time of disease onset**

(**A**) An Oncoprint of 27 patient samples considered to be SHH-MB[3] using the cBioPortal[20, 21] showing the frequency of mutations in *PTEN* and genes that activate the SHH pathway showing co-occurrences. (**B**) Schematic showing Mosaic mutant Analysis with Spatial and Temporal Regulation (MASTR) technique used to model SHH-MB by expressing SmoM2 in scattered GCPs starting at P0 and deleting one or two copies of *Pten* (*Atoh1-FlpoER/+*; *R26*$^{MASTR/LSL\text{-}SmoM2}$; *Pten*$^{fl/fl}$ or *SmoM2-Pten*$^{fl/fl}$ mice). (**C**) Kaplan-Meier curve and statistics (below) for survival of *SmoM2* mice compared to *SmoM2-Pten*$^{fl/fl}$ and *SmoM2-Pten*$^{fl/+}$ mice. Statistics were calculated using the log-rank test. (**D-F**) Representative images of hematoxylin and eosin (H&E) stained sagittal sections of end stage tumors from *SmoM2*, *SmoM2-Pten*$^{fl/+}$, and *SmoM2-Pten*$^{fl/fl}$ mice with higher maginification images shown below (n>8 per genotype). Scale bars indicates 1mm (D-F) and 100 μm (D'-F'). (**G-I**) GFP stained saggital sections of end stage tumors from the the indicated mutants (n=5-8 per genotype). Scale bar indicates 1mm. (**J-L**) Saggital sections of end stage tumors from the indicated mutants stained for PTEN (J-L) or pAKT (**M-O**) with higher magnifications below. Scale bars indicates 1mm (J-O) and 20 μm (J'-O'). (D-O) Dashed lines outline the tumors, solid lines outline IGL, dotted rectangles indicate location of high magnification images.

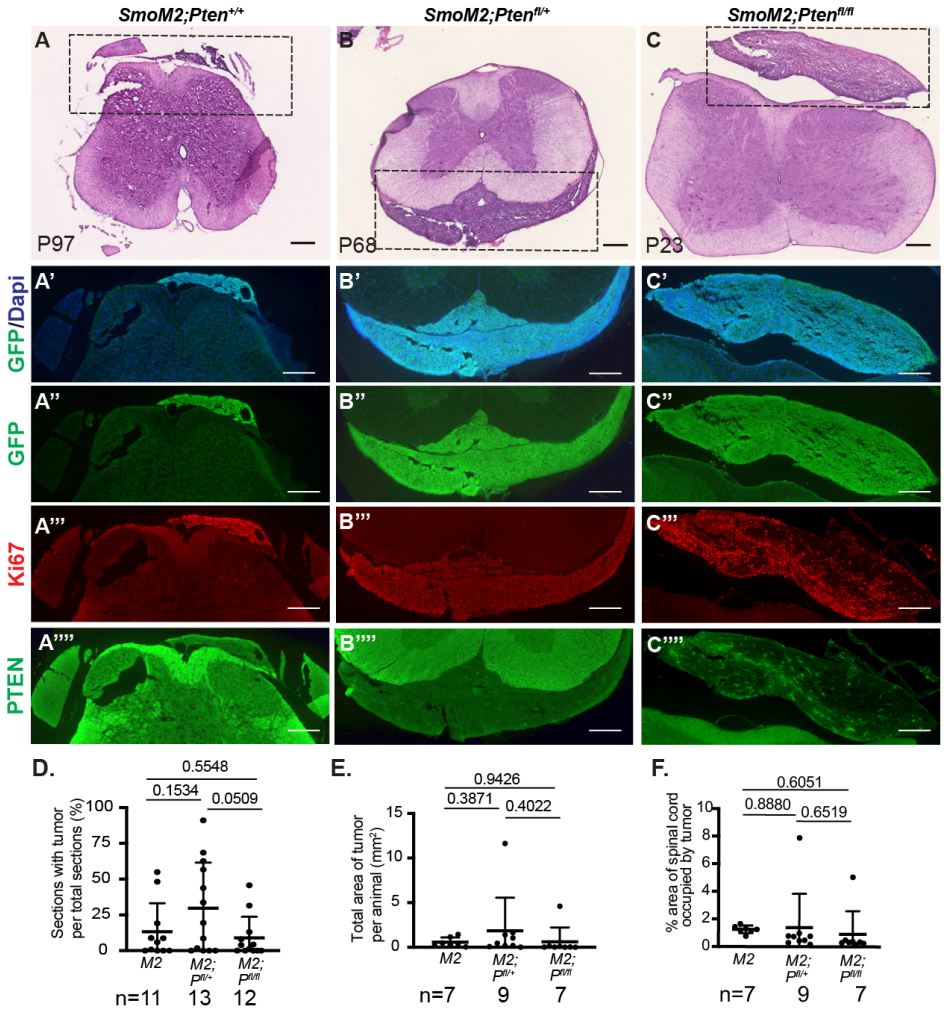

Figure 1–Figure Supplement 1. Loss of *Pten* does not increase metastasis to the spinal cord in *SmoM2* SHH-MB

(**A-C**) Coronal sections of spinal cords stained with H&E from mice of the indicated three genotypes showing metastatic lesions at end stage. Dashed rectangles indicate locations of images below stained for the proteins and DAPI indicated on the left. Scale bars indicates 200μm. (**D**) Quantification of percentage of sections with a tumor for each animal analyzed. (**E**) Quantification of the total area of the tumor on all the sections. (**F**) Quantification of the area of each tumor as a percentage of the spinal cord area in each section. (D-F) Number of animals per genotype (n=) are indicated below graphs. All statistics were determined using an unpaired t-test comparing *SmoM2* tumors to each of the *Pten* mutants or the *Pten* mutants to each other.

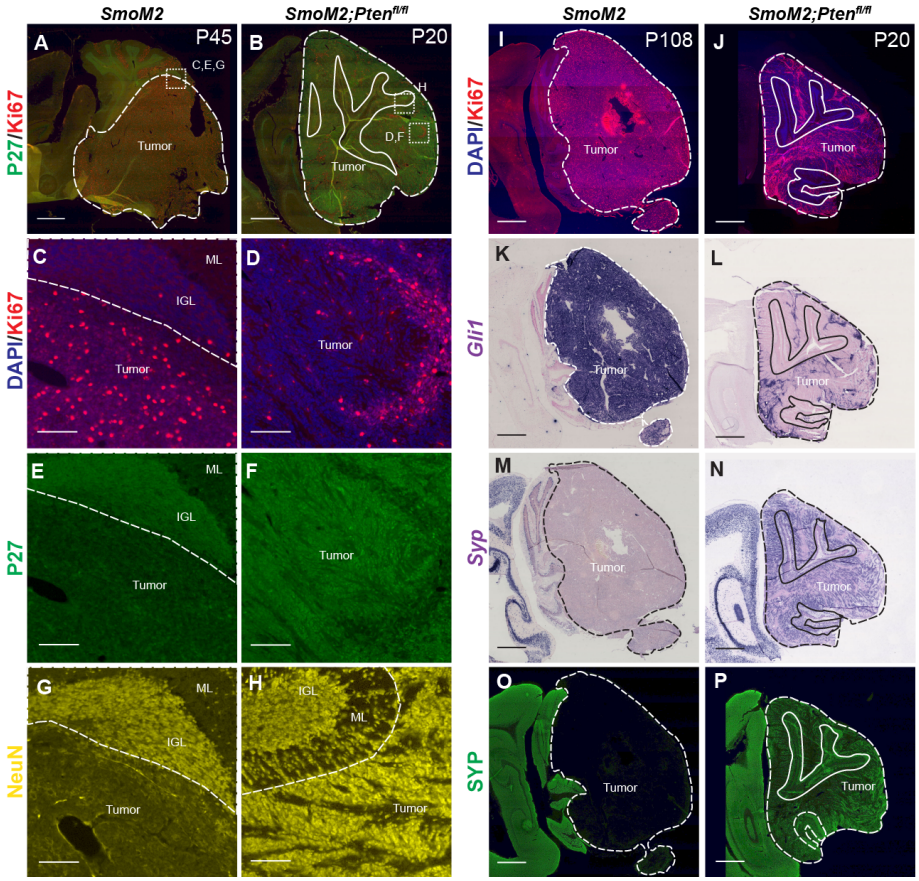

Figure 2. *Pten* loss in *SmoM2* sporadic SHH-MB induces highly differentiated tumors
(**A, B**) Sagittal sections of the cerebellum showing end stage tumors from *SmoM2* and *SmoM2-Pten*$^{fl/fl}$ mice stained for P27 (post mitotic cells) and Ki67 (proliferating cells) (*SmoM2*, n=5; *SmoM2-Pten*$^{fl/fl}$ n=7). Dashed lines outline each tumor, solid lines outline IGL, dotted squared indicate location of high magnification images in (C-H). (**C-H**) High power images of sections stained for Ki67 and DAPI (C, D), P27 (E, F) or NeuN (G, H)(*SmoM2*, n=5; *SmoM2-Pten*$^{fl/fl}$ n=7). Dashed line separates the internal granule layer (IGL) or molecular layer (ML) from the tumor. (**I,J**) Sagittal sections of the cerebellum showing lateral tumors from *SmoM2* and *SmoM2-Pten*$^{fl/fl}$ mice stained for Ki67 and DAPI (*SmoM2*, n=7; *SmoM2-Pten*$^{fl/fl}$ n=8)). (**K-N**) RNA *in situ* hybridization staining of sections for *Gli1* (K, L) and *Syp* mRNA (M, N) (n=3 per genotype). (**O, P**) Immunohistochemical staining of sections for SYP protein (n=6 per genotype). (I-P) Dashed lines outline the tumors, solid lines outline IGL. (A, B, I-P) Scale bars indicate 1mm. (C-H) Scale bars indicates 100μm.

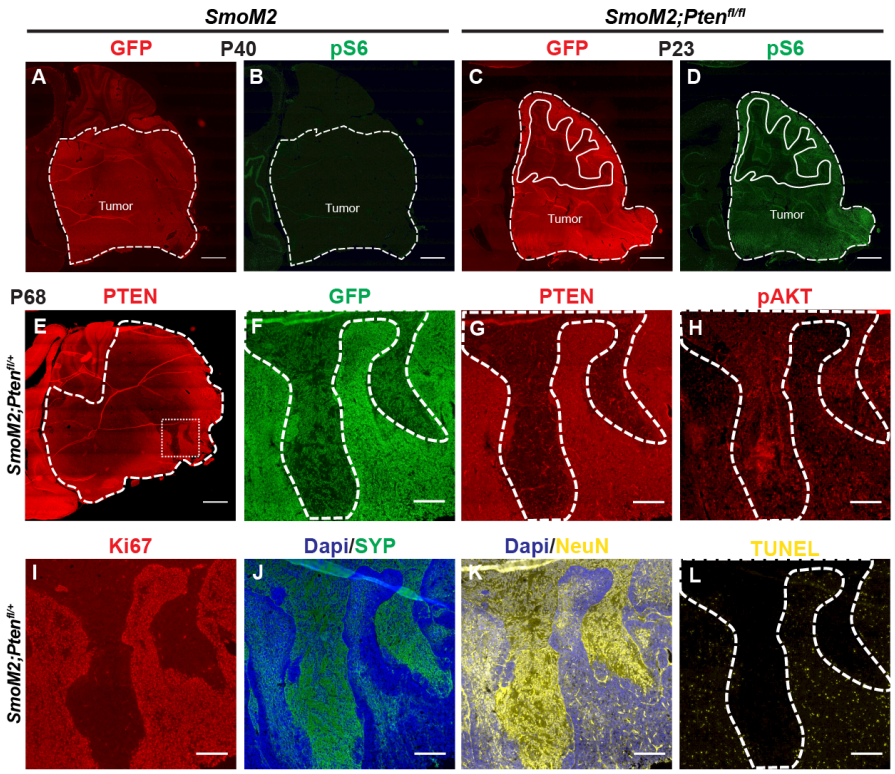

Figure 2–Figure Supplement 1. Spontaneous loss of the second allele of *Pten* in rare cells of some *SmoM2-Pten*$^{fl/+}$ tumors

(**A-D**) Sagittal sections of end stage tumors (GFP+) showing upregulation of pS6 in *SmoM2-Pten*$^{fl/fl}$ mice compared to *SmoM2* (n=3 per genotype). Dashed lines outline the tumors, solid lines outline IGL. Scale bars indicates 1mm. (**E**) Section of end stage tumor from *SmoM2-Pten*$^{fl/+}$ mice showing coherent patches of tumor cells (GFP+) devoid of PTEN (n=3). Dashed line square indicates location of high magnification images shown in (F-L). Scale bar indicates 1mm. (**F-L**) Sections of lateral tumors stained for the indicated protein and DAPI (n=3). Dashed line outlines tumor area where PTEN is absent (G) or pAKT (H), SYP (J) and NeuN (K) are upregulated and proliferation (Ki67) and cell death (TUNEL) are reduced (I, L). Scale bars indicates 200μm.

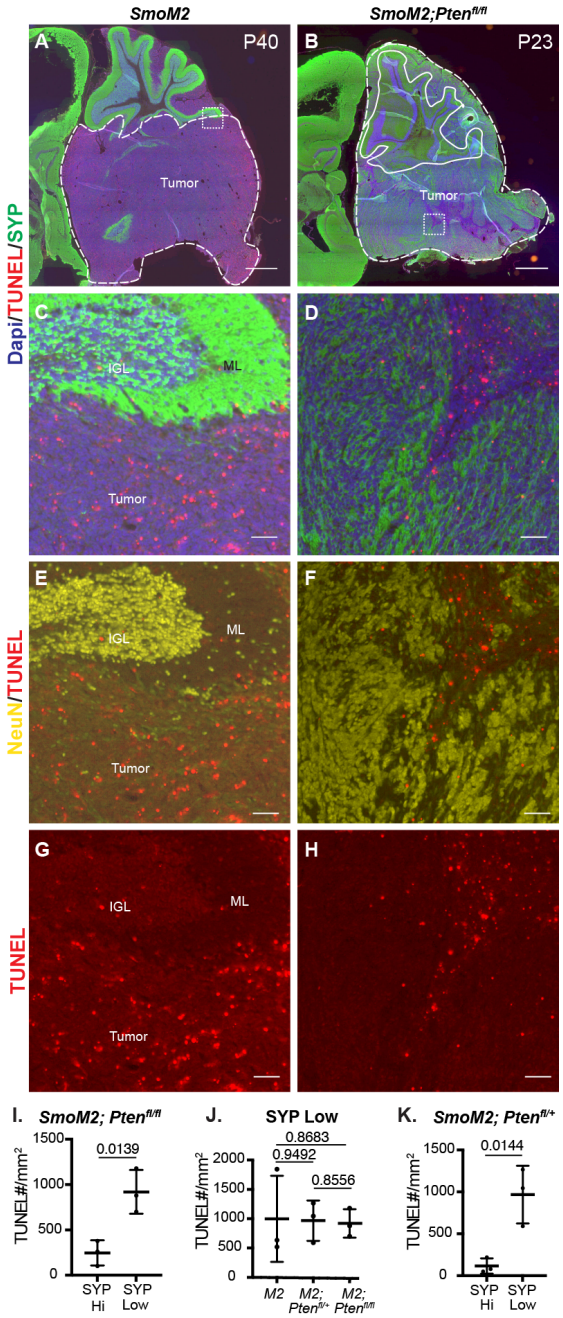

Figure 3. *Pten* loss in *SmoM2* SHH-MB protects differentiated tumor cells from cell death
(**A, B**) Sagittal sections of end stage tumors in *SmoM2* and *SmoM2-Pten*$^{fl/fl}$ mice stained as indicated (*SmoM2*, n=3; *SmoM2-Pten*$^{fl/fl}$ n=4). Dashed lines outline the tumors, solid lines outline IGL. Dotted line square indicates location of high magnification images show in (C-H). Scale bars indicate 1mm. (**C-H**) High magnification images of tumors stained as indicated showing reduced cell death (TUNEL particles) in differentiated regions (NeuN+ and SYP+) of tumors in *SmoM2-Pten*$^{fl/fl}$ mice compared to *SmoM2* (*SmoM2*, n=3; *SmoM2-Pten*$^{fl/fl}$ n=4). Scale bars indicates 50μm. (**I-K**) Quantification of density of TUNEL particles in tumor regions with high SYP (SYP HI) compared to low (SYP Low) staining in *SmoM2-Pten*$^{fl/fl}$ mice (I), in SYP Low regions in *SmoM2* (*M2*), *SmoM2-Pten*$^{fl/+}$ (*M2; Pten*$^{fl/+}$) and *SmoM2-Pten*$^{fl/fl}$ (*M2; Pten*$^{fl/fl}$) mice (J), and in SYP High and Low regions of *SmoM2-Pten*$^{fl/+}$ mice (K).

n=3 mice/genotype. All statistics were determined using an unpaired t-test comparing SYP High to Low (I, K) or two pairs of genotypes (J).

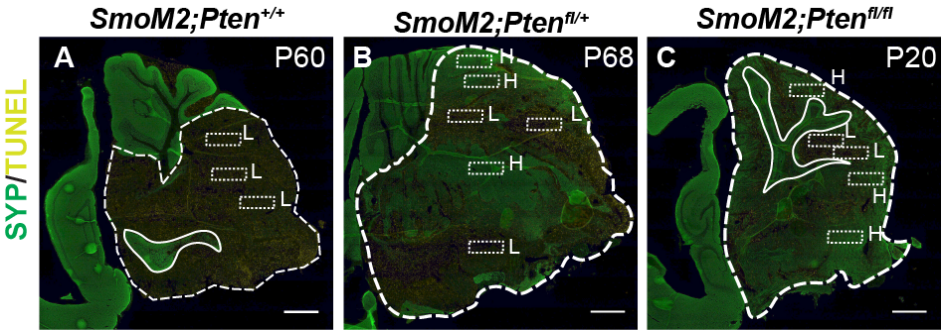

Figure 3–figure supplement 1. Method of quantifying TUNEL particles in tumors
(**A-C**) Examples of stained sagittal cerebellar sections showing where quantifications of density of TUNEL particles were performed in the three genotypes in end stage lateral tumor regions distinguishing high SYP (H) compared to low SYP (L) regions. Dashed lines outline each tumor, solid lines outline IGL, dotted boxes indicate high SYP (H) and low SYP (L) regions. Scale bars indicate 1mm.

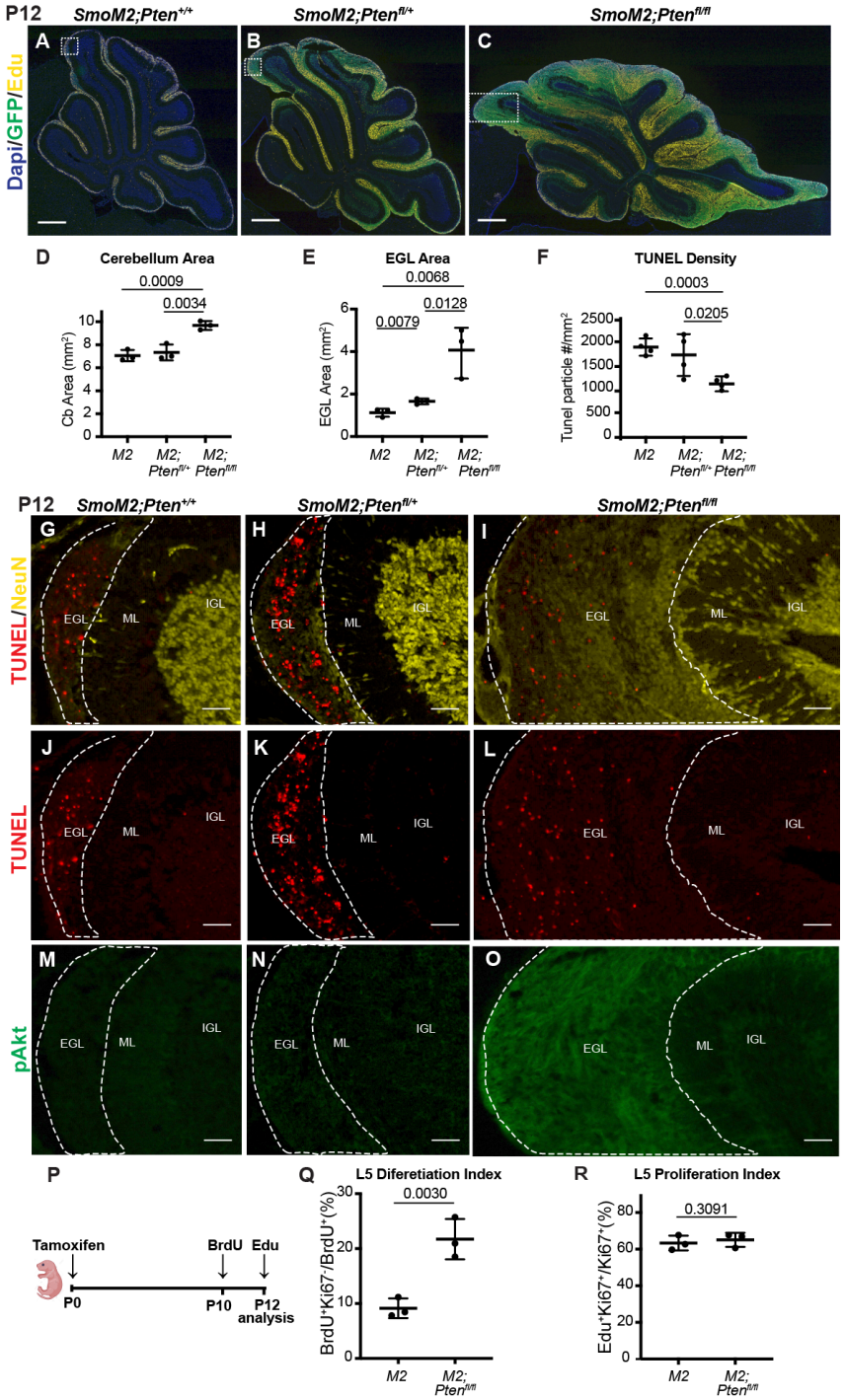

Figure 4. Loss of *Pten* leads to cell autonomous changes in *SmoM2* GCPs at P12

(**A-C**) Midline cerebellar sagittal sections of P12 *SmoM2*, *SmoM2-Pten*$^{fl/+}$ and *SmoM2-Pten*$^{fl/fl}$ mice stained for GFP and EdU to show the EGL with proliferating mutant GCPs (*SmoM2*, n=11; *SmoM2-Pten*$^{fl/+}$ n=5; *SmoM2-Pten*$^{fl/fl}$ n=6). Scale bars indicate 0.5 mm. Dotted line boxes indicate locations of images in (A for G, J, M; B for H, K, N; C for I, L, O). (**D**) Quantification of the area of the cerebellum on midline sections of *SmoM2* (*M2*), *SmoM2-Pten*$^{fl/+}$ (*M2; Pten*$^{fl/+}$) and *SmoM2-Pten*$^{fl/fl}$ (*M2; Pten*$^{fl/fl}$) mice (n=3 mice/genotype). (**E**) Quantification of the area of the EGL on midline sections in the three genotypes (n=3 mice/genotype). (**F**) Quantification of TUNEL particle density (cell death) in the EGL of midline

sections in the three genotypes (n=3 mice/genotype). (**G-O**) Staining of sections of the three genotypes for the proteins indicated showing reduced cell death (TUNEL density) and increased pAKT and NeuN in the EGL of *SmoM2-Pten*$^{fl/fl}$ mice (n>3 per genotype). Scale bars indicates 50μm. EGL, external granule layer; ML, molecular layer (region between IGL and EGL); IGL, internal granule layer. (**P**) Schematic of experimental design. (**Q**) Quantification of the percentage of proliferating GCPs that became post mitotic (Ki67-) between BrdU labeling at P10 and analysis at P12 in a region of lobule 5 (L5) (n=3 mice/genotype). (**R**) Quantification of the percentage of GCPs that are in S phase (EdU+ Ki67+ of all Ki67+ GCPs) at P12 (n=3 mice/genotype). All statistics were determined using an unpaired t-test comparing two pairs of genotypes.

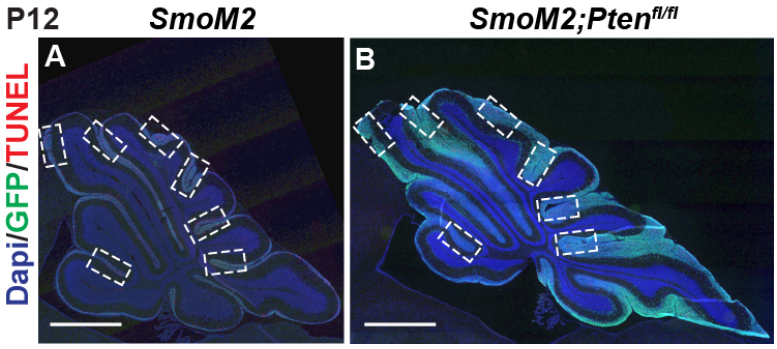

Figure 4–figure supplement 1. Method of quantifying TUNEL particles in P12 EGL
(**A, B**) Examples of stained midline sagittal cerebellar sections showing where quantification of density of TUNEL particles was performed in the EGL in medial regions of the cerebellum. Scale bars indicate 1mm.

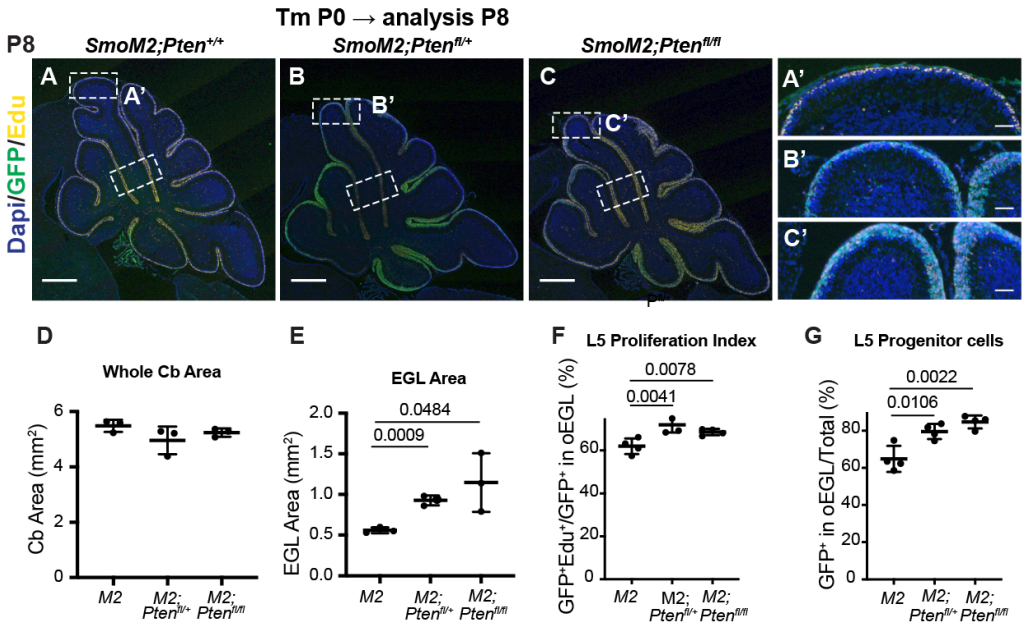

Figure 5. Loss of *Pten* leads to cell autonomous changes *SmoM2* GCP behaviors at P8
(**A-C**) Midline cerebellar sagittal sections of P8 *SmoM2*, *SmoM2-Pten*$^{fl/+}$ and *SmoM2-Pten*$^{fl/fl}$ mice stained for GFP and EdU to show the EGL with proliferating mutant GCPs. Dotted line boxes indicate locations of where quantifications were performed. Scale bars indicate 0.5 mm. (A'-C') High magnification images of areas indicated in (A-C). Scale bars indicate 0.5μm. (**D**) Quantification of the area of the cerebellum on midline sections of *SmoM2* (*M2*), *SmoM2-Pten*$^{fl/+}$ (*M2; Pten*$^{fl/+}$) and *SmoM2-Pten*$^{fl/fl}$ (*M2; Pten*$^{fl/fl}$) mice (n=3 mice/genotype). (**E**) Quantification of the area of the external granule layer (EGL) on midline sections in the three genotypes (n=3 mice/genotype). (**F**) Quantification of the proliferation index in lobule 5 (L5) at P8: percentage of mutant GCPs that are in S phase (GFP+ EdU+ of all GFP+ GCPs), (n=4 mice/genotype). (**G)** Quantification of the percentage of mutant GCPs that remained in the proliferative outer EGL (oEGL) at P8 and thus were progenitors. Analysis performed in wall of lobule 5 (lower rectangles in (A-C) (n=4 mice/genotype). All statistics were determined using an unpaired t-test comparing two pairs of genotypes.

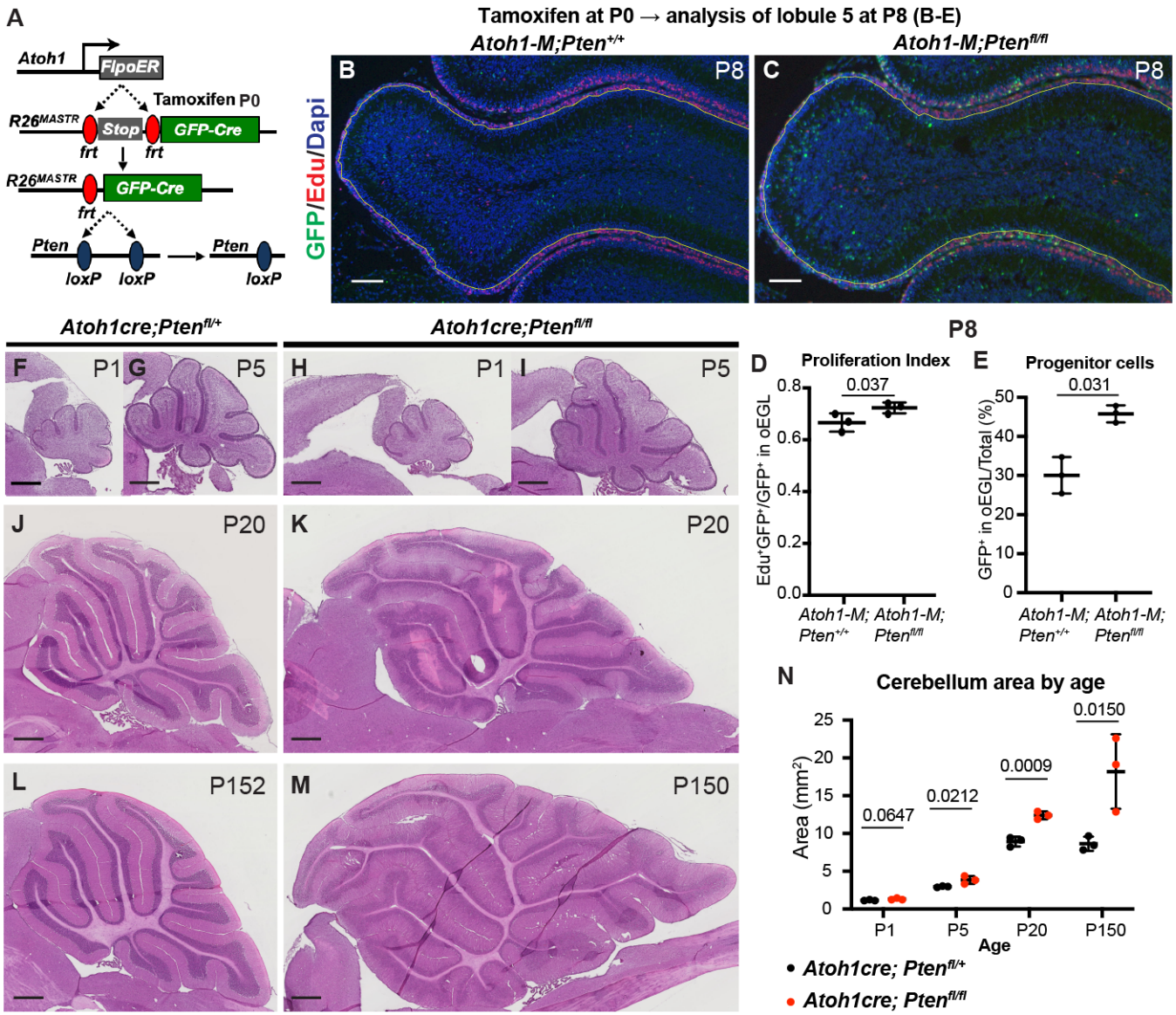

Figure 6. Loss of *Pten* in normal GCPs causes increased proliferation and decreased differentiation

(**A**) Schematic showing mosaic mutant analysis approach to study scattered GFP+ *Pten* homozygous mutant GCPs in *Atoh1-FlpoER/+*; *R26*$^{FSF\text{-}GFPcre/+}$; *Pten*$^{fl/fl}$ (*Atoh1-M-Pten*$^{fl/fl}$) mice compared to control GFP+ cells in *Atoh1-FlpoER/+*; *R26*$^{FSF\text{-}GFPcre/+}$; *Pten*$^{+/+}$ mice (*Atoh1-M- Pten*$^{+/+}$) at P8 following tamoxifen at P0. (**B, C**) Midline sagital sections of lobule 5 stained with GFP marking mutant cells and EdU (S phase) at P8 in the two genotypes. Scale bars indicates 100μm. (**D**) Quantification of the proliferation index in lobule 5 (L5) at P8: percentage of mutant GCPs that are in S phase (GFP+ EdU+ of all GFP+ GCPs; n=3 mice per genotype). (**E**) Quantification of the percentage of mutant GFP+ GCPs that remained in the proliferative outer EGL (oEGL) at P8 and thus were progenitors (n=3 mice per genotype). (**F-M**) Midline sagittal H&E stained sections of the cerebellum of conditional mutant mice lacking *Pten* in the GCP lineage (*Atoh1-Cre*; *Pten*$^{fl/fl}$) compared to controls (*Atoh1-Cre*; *Pten*$^{fl/+}$). Scale bars indicates 500μm. (**N**) Quantification of the area of midline sagittal sections of the cerebellum across development and aging (n=3 mice per age). All statistics were determined using an unpaired t-test comparing two pairs of genotypes (D, E) or two genotypes at each age (N).

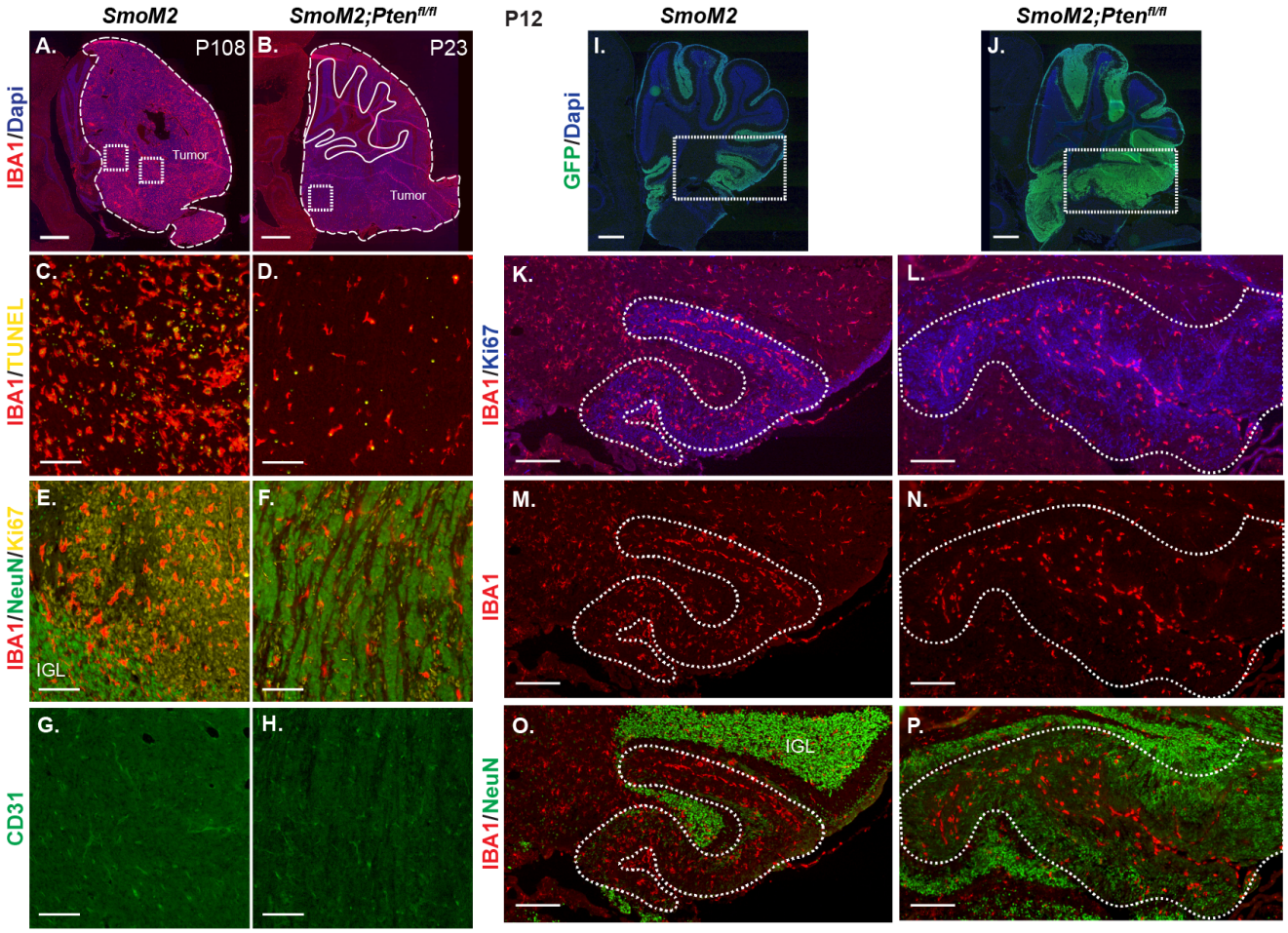

Figure 7. Loss of *Pten* in *SmoM2* GCPs results in a cell non-autonomous decrease in macrophages in SHH-MB tumors

(**A, B**) Sagittal sections of end stage tumors in *SmoM2* and *SmoM2-Pten$^{fl/fl}$* mice stained with IBA1 (macrophage marker) and DAPI (n=3 mice/genotype). Dashed lines outline the tumors, solid lines outline IGL. Dotted line squares indicate locations of high magnification images show in (C-H). Scale bars indicate 1mm. (**C-H**) Higher magnification images of tumors stained with IAB1 and TUNEL (C, D), IAB1, NeuN and Ki67 showing enrichment of macrophages in undifferentiated regions of *SmoM2-Pten$^{fl/fl}$* mice (E, F) and with CD31 to label blood vessels (G, H) (n=5-9 mice/genotype). IGL, internal granule layer. Scale bars indicates 100μm. (**I, J**) Lateral sagittal cerebellar sections of P12 *SmoM2* and *SmoM2-Pten$^{fl/fl}$* mice stained for GFP and DAPI to show the EGL with mutant GCPs (n=3 mice/genotype). Dotted line boxes indicate locations of higher magnifications images in (K-P). Scale bars indicate 500μm. (**K-P**) Sections of P12 mice stained with IAB1, Ki67 and NeuN showing macrophages in large tumor lesions are enriched in proliferative regions of *SmoM2-Pten$^{fl/fl}$* mice (n=3 mice/genotype). Dotted line outlines the tumor lesion. Scale bars indicate 200μm.

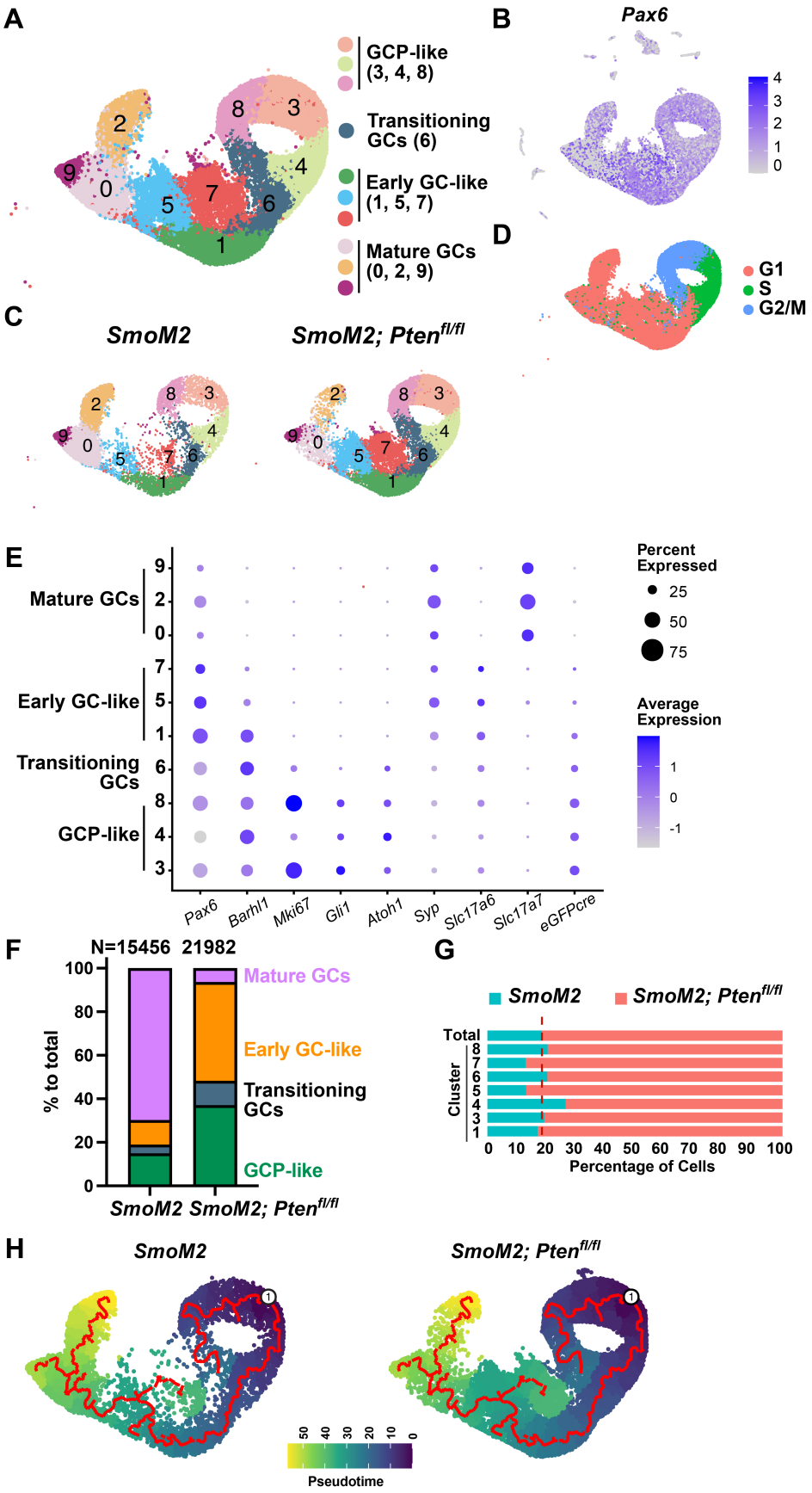
A
GCP-like (3, 4, 8)
Transitioning GCs (6)
Early GC-like (1, 5, 7)
Mature GCs (0, 2, 9)
B
Pax6
D
G1
S
G2/M
C
SmoM2
SmoM2; Pten fl/fl
E
Mature GCs
Early GC-like
Transitioning GCs
GCP-like
Pax6
Barhl1
Mki67
Gli1
Atoh1
Syp
Slc17a6
Slc17a7
eGFPcre
Percent Expressed
Average Expression
F
N=15456 21982
% to total
Mature GCs
Early GC-like
Transitioning GCs
GCP-like
SmoM2
SmoM2; Pten fl/fl
G
SmoM2
SmoM2; Pten fl/fl
Total
Cluster
Percentage of Cells
H
SmoM2
SmoM2; Pten fl/fl
Pseudotime

Figure 8. scRNA-seq analysis of tumors from *SmoM2* and *SmoM2-Pten*$^{fl/fl}$ mice reveals altered differentiation in SHH-MB tumor cells lacking *Pten*

(**A**) UMAP of integrated cells from *SmoM2* (n=2) and *SmoM2-Pten*$^{fl/fl}$ (n=2) tumors showing scRNA-seq GCP-lineage clusters 0-9 (*Pax6*-expressing) (left) and the assignment of cell types to each cluster (right) based on marker gene expression and cell cycle phase. (**B**) *Pax6* expression (GCP-lineage marker) shown across all clusters in UMAP of all tumor cells. (**C**) UMAP of GCP-lineage cells shown by genotye. (**D**) UMAP of GCP-lineage cells (two genotypes) showing cell cycle phases. (**E**) Dot plot graph showing expression levels of GCP-lineage marker genes and desgnation of the clusters as GCP-like or maturing GC-like cell types. (**F**) Graph of GCP-lineage cells showing percentage of cells from each genotype that are GCP-like, transitioning GC-like, early GC-like and mature GC-like showing a higher percentage of mature GCs in tumors from *SmoM2* mice. (**G**) Graph showing proportions of cells of each genotype in each of the GCP-lineage cell types excuding mature GCs that are mostly from *SmoM2* mice. Dotted line represents the expected ratio between the two genotypes. (**H**) Pseudotime analysis reflecting the differentiation pathway of cells within the GCP-lineage with an origin in the GCP-like clusters, indicating cluster 7 is stalled or altered during differentiation.

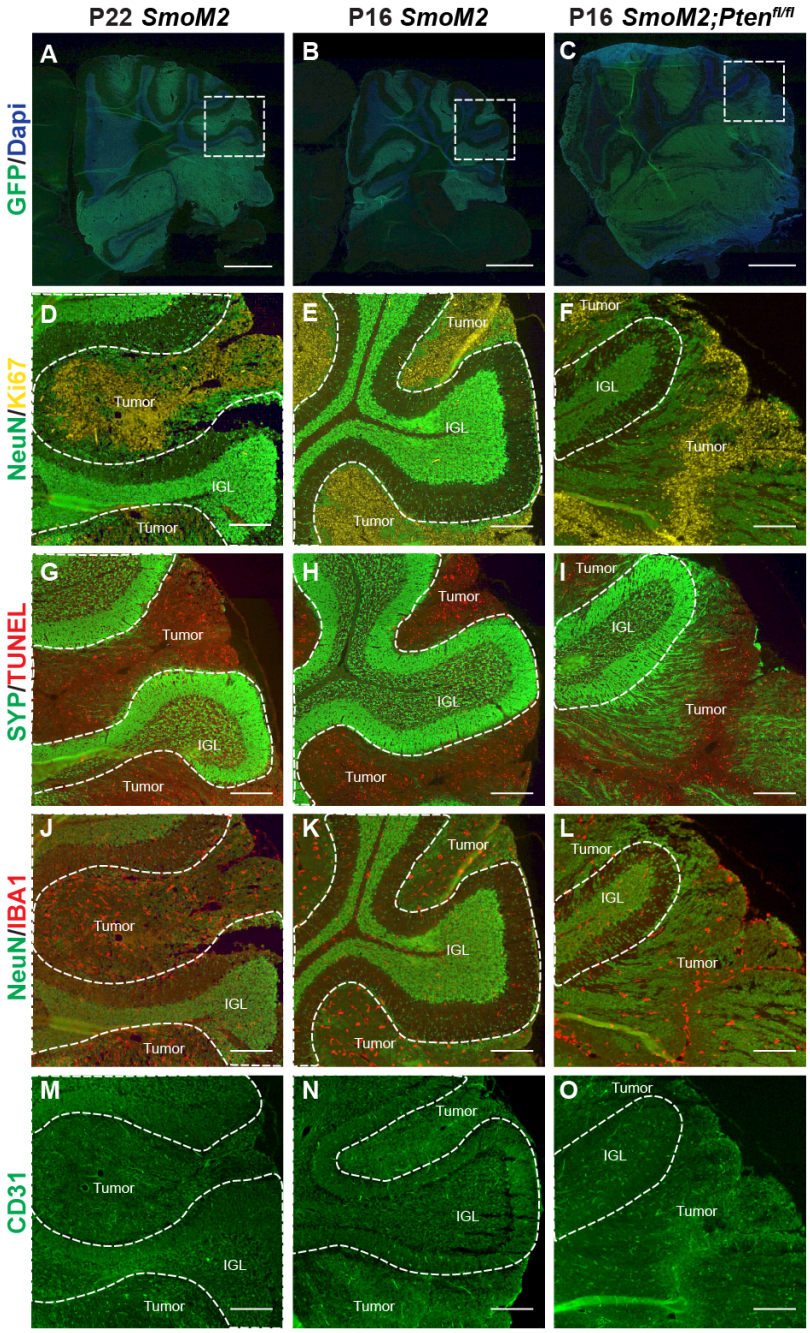

Figure 8–figure supplement 1 The cellular phenotypes of large tumors from P16 *SmoM2-Pten*$^{fl/fl}$ mice and P22 *SmoM2* mice are similar to end stage

(**A-C**) Sagittal sections of cerebellar sections from P16 and P22 *SmoM2* mice and P16 *SmoM2-Pten*$^{fl/fl}$ mice stained with GFP and DAPI to highlight tumor cells (n=3 mice/genotype). Dashed line squares indicate location of high magnification images shown in (D-O). Scale bars indicate 1mm. (**D-O**) Higher magnification images of tumors stained for indicated proteins to confirm that the cellular phenotypes of large tumors in P16 *SmoM2-Pten*$^{fl/fl}$ mice and P22 *SmoM2* mice are like tumors at end stage. Dashed lines outline the internal granule layer (IGL). Scale bars indicate 200μm.

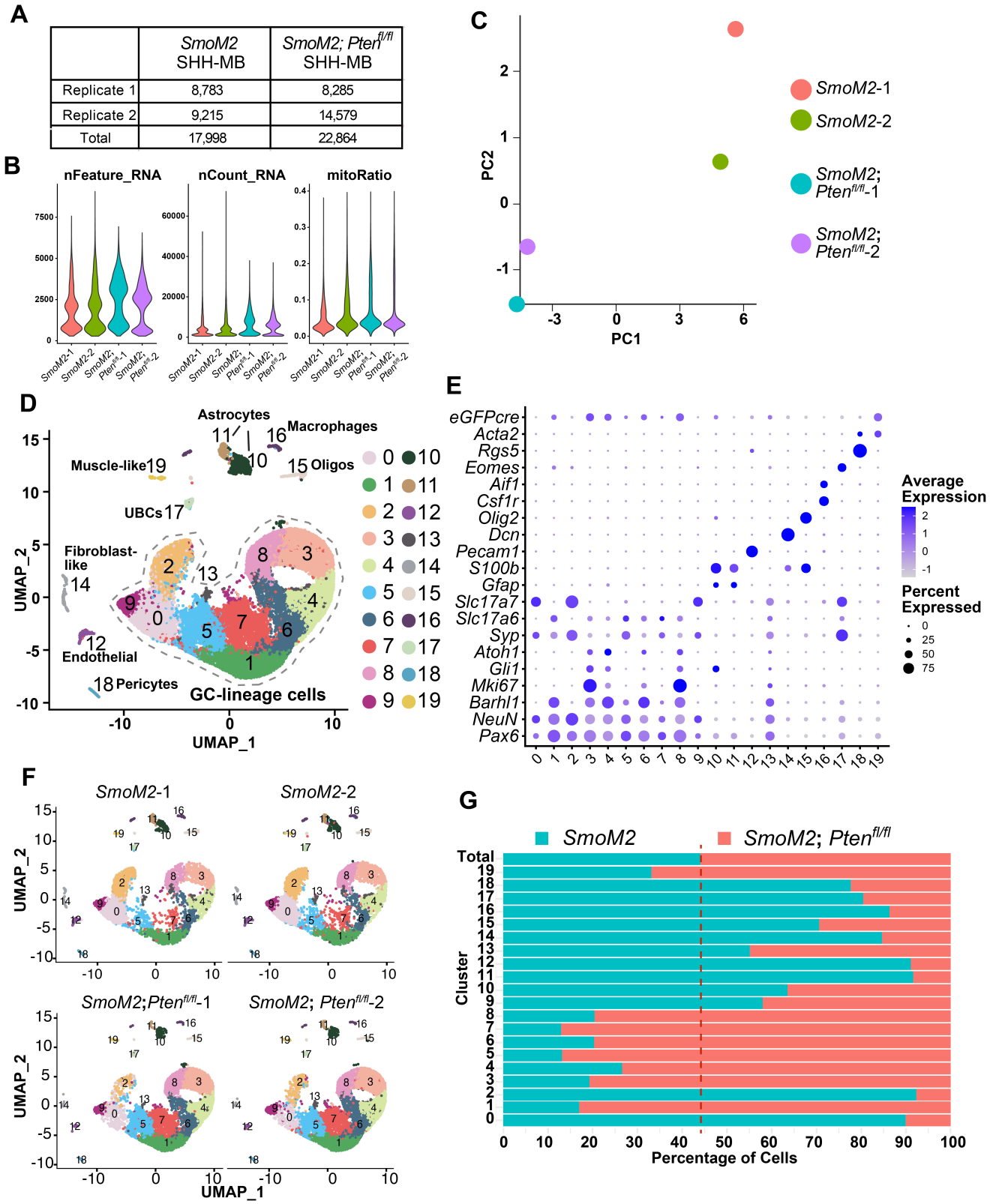

Figure 8–figure supplement 2. ScRNA-seq comparison of tumors from P16 *SmoM2-Pten*$^{fl/fl}$ mice to P22 *SmoM2* mice

(**A**) Number of cells from each replicate and genotype used for downstream analyses after filtering. (**B**) Violin plots showing the number of features, and RNA counts and percent mitochondrial RNA counts across the biological replicates of the scRNA-seq data set after filtering out poor quality cells (where number of detected genes was ≤ 500, the number of detected transcripts was ≥ 18,000 and mitochondrial gene percentage ≥ 20%). (**C**) PCA plot after filtering out poor quality cells and integrating the replicates and genotypes showing the two genotypes separate well. (**D**) UMAP showing projections of all cells showing cluster annotations. (**E**) Dot plot graph showing expression levels of cell type marker genes across all clusters and their cell type desgnations. (**F**) UMAPs of all cells shown by genotype and sample. (**G**) Graph showing proportions of cells of each genotype when all cells are included. Dotted line represents the expected ratio between the two genotypes.

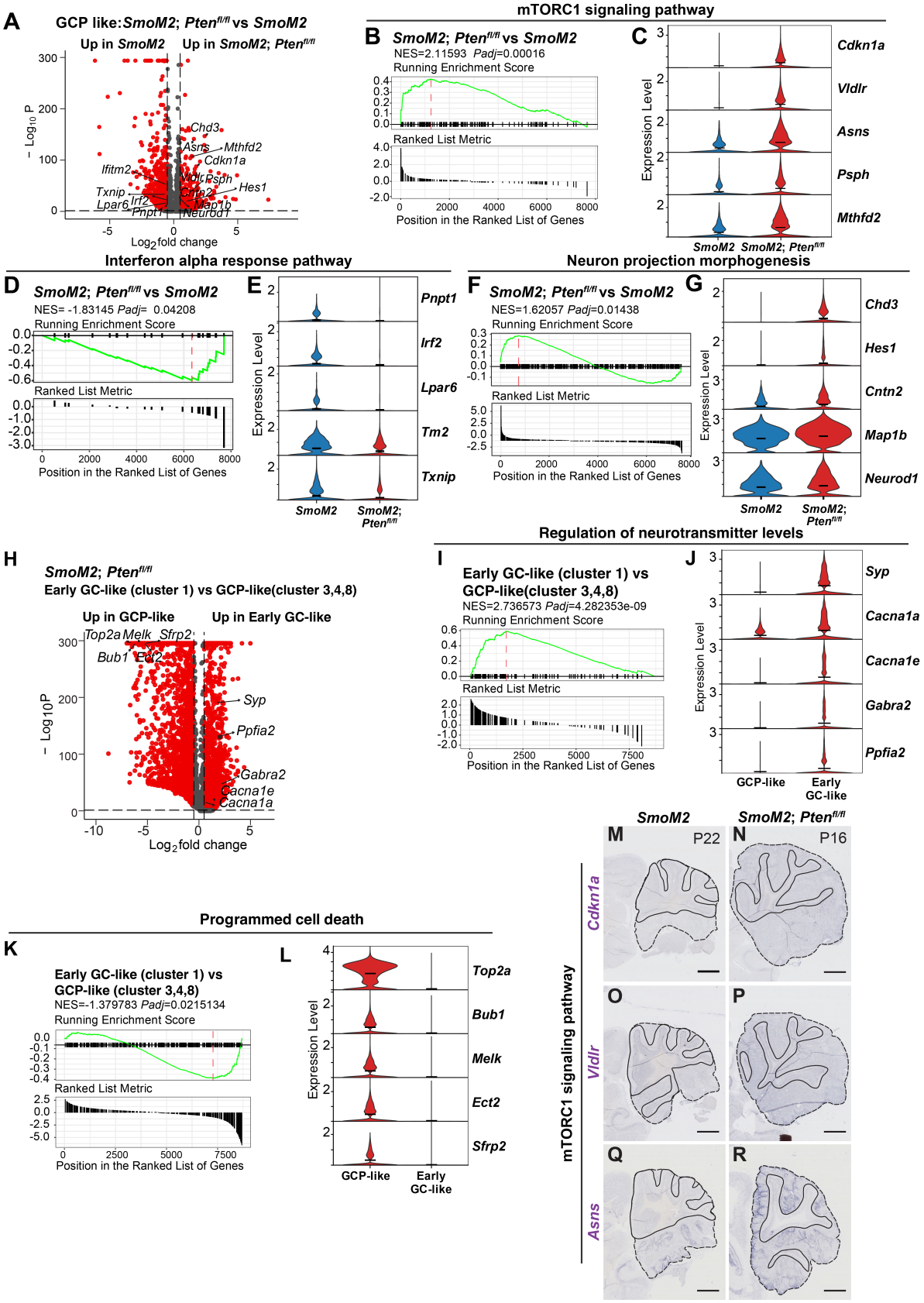

Figure 9. *SmoM2* tumors lacking *Pten* have altered neurogenesis and immune signaling

(**A**) Volcano plot showing differentially expressed genes in GCP-like tumor cell clusters (3, 4, 8) (red: adjusted p-value <0.05, ab[$\log_2$fold-change]>0.5), in *SmoM2-Pten*$^{fl/fl}$ tumors compared to *SmoM2*. (**B**) Gene set enrichment analysis (GSEA) plots (Hallmark terms) showing that mTORC1 signaling pathway is significantly unregulated in *SmoM2-Pten*$^{fl/fl}$ tumors compared to *SmoM2*. (**C**) Violin plots showing expression levels of mTORC1 signaling pathway genes in the two genotypes. (**D**) GSEA plots (Hallmark terms) showing that Interferon alpha response is significantly downregulated in *SmoM2-Pten*$^{fl/fl}$ tumors compared to *SmoM2*. (**E**) Violin plots showing expression levels of Interferon alpha response genes in the two genotypes. (**F**) GSEA plots of Gene ontology (GO) terms (biological processes) showing that regulation of neural differentiation is significantly upregulated in *SmoM2-Pten*$^{fl/fl}$ tumors compared to *SmoM2*. (**G**) Violin plots showing expression levels of neural differentiation genes in the two genotypes, indicating an early stage of neurogenesis is enhanced. (**H**) Volcano plot showing differentially expressed genes in early GC-like cluster 1 compared to GCP-like cell clusters (3, 4, 8) in *SmoM2-Pten*$^{fl/fl}$ tumors (red: adjusted p-value <0.05, ab[$\log_2$fold-change]>0.5). (**I**) GSEA plots of Gene ontology (GO) terms (biological processes) confirmed upregulation of neural differentiation in cluster 1 compared to the GCP-like cell clusters. (**J**) Violin plots showing expression levels of neural differentiation genes in the two cell types. (**K**) GSEA plots of Gene ontology (GO) terms (biological processes) showed downregulation of 'positive regulation of programmed cell death' in cluster 1 compared to the GCP-like cell clusters. (**L**) Violin plots showing expression levels of programmed cell death genes in the two cell types. (**M-R**) Lateral sagittal sections of tumors from *SmoM2* mice (P22, M, O, Q) or *SmoM2-Pten*$^{fl/fl}$ mice (P16, N, P, R) stained for RNA in situ analysis of *Cdkn1a*, *Vldr*, *Asns*, indicating upregulation of mTORC1 signaling pathway in *Pten* mutant tumors.

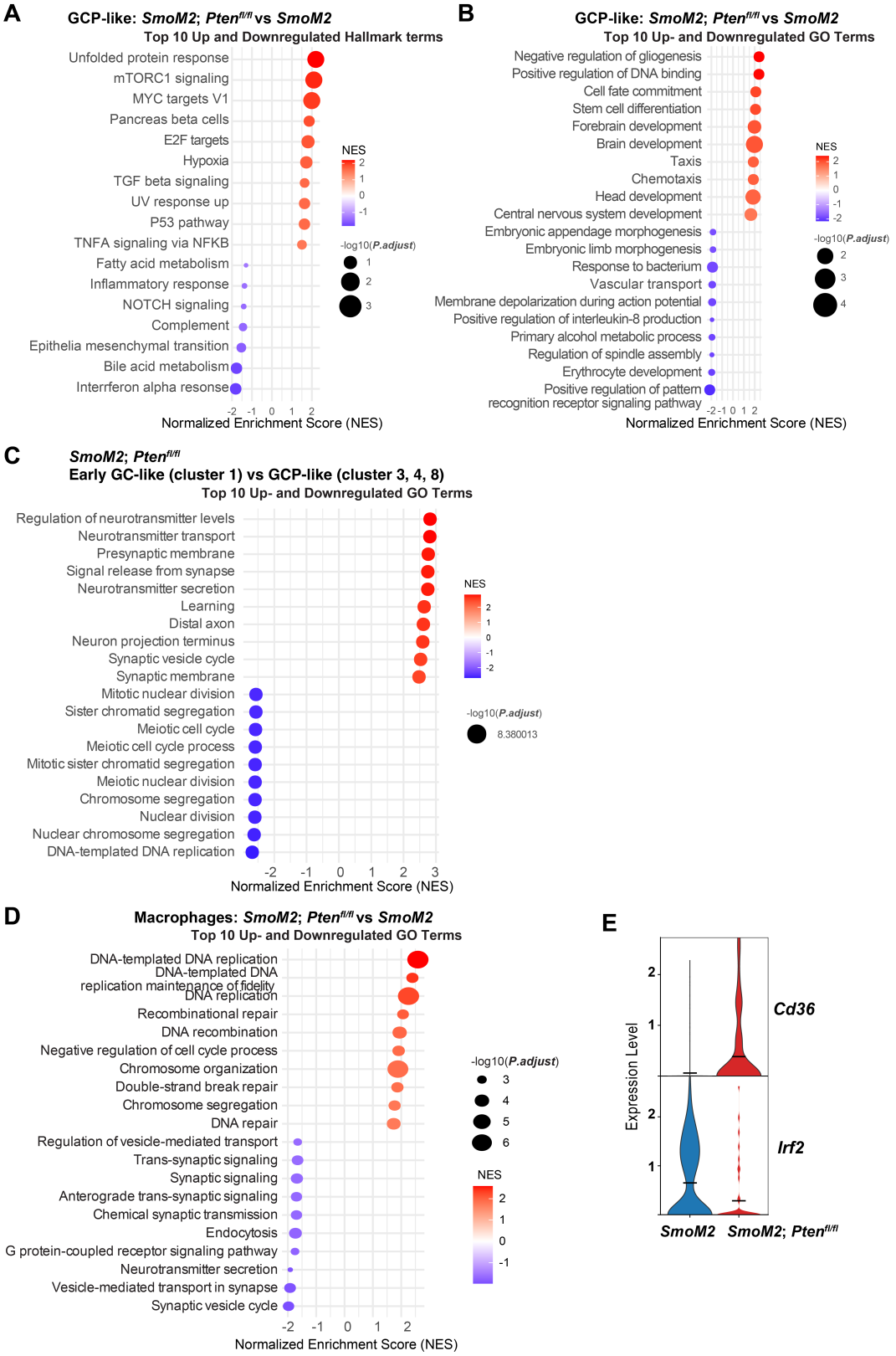

Figure 9–figure supplement 1. Differential expression analyses confirms activation of mTOR signaling, altered neural differentiation and decreased immune signaling following *Pten* loss

A. Bar plots showing top 10 upregulated and downregulated Hallmark terms in *SmoM2-Pten*$^{fl/fl}$ GCP-like cells compared to *SmoM2*. **B**. Bar plots showing top 10 upregulated and downregulated Gene ontology (GO) terms (biological processes) in GCP-like cells from *SmoM2-Pten*$^{fl/fl}$ mice compared to *SmoM2*. **C**. Bar plots showing top 10 upregulated and downregulated Gene ontology (GO) terms (biological processes) in early GC-like cluster 1 compared to GCP-like cell clusters (3, 4, 8) in *SmoM2-Pten*$^{fl/fl}$ tumors. **D**. Bar plots showing the top 10 upregulated and downregulated Gene ontology (GO) terms (biological processes) in macrophages in *SmoM2-Pten*$^{fl/fl}$ tumors compared to *SmoM2*. **E.** Violin plots showing expression levels of *Cd36* and *Irf2* in macrophages in the two tumor genotypes.